Ice in Clouds Experiment—Layer Clouds. Part I: Ice Growth Rates Derived from Lenticular Wave Cloud Penetrations

ANDREW J. HEYMSFIELD,* PAUL R. FIELD,+ MATT BAILEY,# DAVE ROGERS,* JEFFREY STITH,* CYNTHIA TWOHY,@ ZHIEN WANG,& AND SAMUEL HAIMOV&

* *NCAR, Boulder, Colorado*
+ *Met Office, Exeter, United Kingdom*
# *Desert Research Institute, Reno, Nevada*
@ *Oregon State University, Corvallis, Oregon*
& *University of Wyoming, Laramie, Wyoming*

(Manuscript received 21 December 2010, in final form 20 May 2011)

ABSTRACT

Lenticular wave clouds are used as a natural laboratory to estimate the linear and mass growth rates of ice particles at temperatures from −20° to −32°C and to characterize the apparent rate of ice nucleation at water saturation at a nearly constant temperature. Data are acquired from 139 liquid cloud penetrations flown approximately along or against the wind direction. A mean linear ice growth rate of about 1.4 μm s^{-1}, relatively independent of particle size (in the range 100–400 μm) and temperature is deduced. Using the particle size distributions measured along the wind direction, the rate of increase in the ice water content (IWC) is calculated from the measured particle size distributions using theory and from those distributions by assuming different ice particle densities; the IWC is too small to be measured. Very low ice effective densities, <0.1 g cm^{-3}, are needed to account for the observed rate of increase in the IWC and the unexpectedly high linear growth rate.

Using data from multiple penetrations through a narrow (along wind) and thin wave cloud with relatively flat airflow streamlines, growth rate calculations are used to estimate where the ice particles originate and whether the ice is nucleated in a narrow band or over an extended period of time. The calculations are consistent with the expectation that the ice formation occurs near the leading cloud edge, presumably through a condensation–freezing process. The observed ice concentration increase along the wind is more likely due to a variation in ice growth rates than to prolonged ice nucleation.

1. Introduction

Primary ice nucleation and secondary ice production processes are poorly understood. They are driven by thermodynamics and aerosol properties, they are affected by natural and anthropogenic sources, and the need for better understanding is evidenced by large uncertainties in the ability to model precipitation production and to predict climate changes. Heterogeneous freezing on ice nuclei (IN) is thought to initiate the ice phase in most clouds at temperatures between about −5° and −38°C, but it is poorly known where and how the ice particles are first formed and which aerosol particles are important as IN for most clouds. Identification of ice just after its production is observationally difficult. Measurements in clouds have lacked the resolution to sample adequately early ice in clouds or the nuclei that influence ice crystal formation. Crystal concentrations are often below the 1–10-L^{-1} detection level of most modern particle probes; and if the crystals are produced through drop freezing, their quasi-spherical shapes render them difficult to distinguish from water droplets.

Only under simple growth conditions is it possible to investigate the initial and early development of ice particles. Lenticular wave clouds are an attractive target because the particles can develop in a laboratory-like thermodynamic environment. Wave clouds develop over a wide range of temperatures and with weak to strong vertical velocities, thus simulating the updraft conditions in more complex convective cloud environments. In addition, their quasi-steady-state behavior allows ice

Corresponding author address: Andrew Heymsfield, National Center for Atmospheric Research, P. O. Box 3000, Boulder, CO 80307.
E-mail: heyms1@ucar.edu

DOI: 10.1175/JAS-D-11-025.1

processes to be studied over an extended period when repeated penetrations of the cloud can be made with instrumented aircraft.

a. Results from lenticular wave cloud studies

What can be learned from nearly constant altitude penetrations from the upwind to downwind regions of wave clouds that would complement observations of early ice particle development derived from laboratory experiments? Particle habit change with time and temperature is a good example. Baker and Lawson (2006) describe observations of ice particles that grew in wave clouds at temperatures between −15° and −60°C, with the bulk of the observations between −20° and −40°C. They found the dominant crystal type by mass to be polycrystals—they refer to them as the rosette shape—including pristine bullet rosettes, mixed-habit rosettes, rosettes with side planes, and platelike polycrystals. They also found budding rosettes (<200 μm in diameter, with relatively short bullets) and small and large irregular habits. Plates were rarely observed. The riming threshold sizes for wave cloud particles were characterized: column widths of about 50–80 μm with corresponding lengths of about 125–300 μm, bullet rosette diameters from 100 to 300 μm, and side planes of about the same as the rosette size range.

These findings are consistent with the laboratory studies of Bailey and Hallett (2004, 2009, hereafter BH04 and BH09) at water saturation but without the presence of cloud droplets, where platelike polycrystals were observed to dominate the habit distribution between −20° and −40°C, and bullet rosettes and columns predominated at temperatures below −40°C. According to BH04 and BH09, bullet rosettes that fall to warmer platelike growth temperatures, in the absence of riming, develop side planes from the core of the polycrystal where platelike structures emerge when stimulated to grow by the warmer platelike growth temperature. A distinction between the BH04/BH09 studies and those of Baker and Lawson (2006) likely has to do with the presence of droplets. As suggested by the latter authors, side plane–type crystals can develop their characteristic structure from sites of riming on the substrates of crystals of other types (columns, rosettes).

Wave clouds provide ideal environments for characterizing the mode(s) of ice nucleation and the sources of the ice nuclei. These are achieved by measuring ice number concentration and residuals of aerosols that populate the cloud ice (e.g., Twohy and Poellot 2005) as a function of the location and time that parcels have resided in the liquid water region as a function of temperature, and relating them to aerosol and IN source regions. For temperatures above about −38°C, earlier observations in European wave clouds suggested a limited role for deposition nucleation (e.g., Field et al. 2001). They asserted that heterogeneous nucleation occurs in the supercooled liquid water region; the ice grows and then remains in the descending part of the wave as the droplets evaporate (Cooper and Vali 1981; Field et al. 2001; Baker and Lawson 2006). For one lenticular cloud studied during the Ice in Clouds Experiment—Layer Clouds (ICE-L), observations and modeling indicate that ice crystals formed by freezing of deliquescent cloud condensation nuclei and/or immersion freezing, with a concentration of aerosol larger than 0.5 μm, were a good predictor of ice nuclei concentrations (Eidhammer et al. 2010). Dust aerosols that derived from dry lake beds located in the Great Basin region in Utah acted as the primary ice nuclei in another ICE-L wave cloud (Pratt et al. 2010). In ICE-L clouds, Twohy et al. (2010) showed a positive correlation among large aerosols, biomass burning aerosol types, heterogeneous IN, and ice concentrations in wave clouds. DeMott et al. (2010) noted that aerosol particles larger than 0.5 μm were strongly correlated with ice nuclei concentrations in diverse geographical regions of the globe.

Prior to ICE-L, observations by Field et al. (2001) and references cited therein indicated that ice formed in the descending branch of the wave cloud and suggested a role for evaporation freezing by contact nucleation occurring from inside the droplet (referred to as "inside-out"; Durant and Shaw 2005). However, such an association has not yet been found for the ICE-L data. Using a 1D kinematic model to simulate ice production in 30 of the wave cloud penetrations during ICE-L, Part II of this study (Field et al. 2010, manuscript submitted to *J. Atmos. Sci.*; hereafter Part II) finds a positive correlation between modeled concentrations of ice particles and the concentration of aerosols larger than 0.5 μm, for a condensation or immersion freezing mechanism.

Wave clouds additionally provide an environment to evaluate airborne instrumentation, thereby facilitating the characterization of the wave cloud growth environment. Relative humidities measured by probes employing different techniques can be readily evaluated, using water and ice saturated conditions in the upward and downward moving branches of the waves, respectively, as reference points (Heymsfield and Miloshevich 1995). Ice water content (IWC) and particle size distribution (PSD) measurements along wave cloud streamlines can be evaluated directly (Gerber et al. 1998), and measurements from different probes covering the same size range can be evaluated directly and against each other (see section 3). By making ice nuclei measurements upwind of a wave cloud and ice concentrations within the cloud, IN measurement techniques can be evaluated (DeMott

et al. 1998). Furthermore, agreement between the IN counter results and the model-derived IN concentrations in Part II suggests that freezing rates are rapid enough for the short residence time of the IN counter to be effective for temperatures colder than −24°C.

Wave clouds provide an environment for measuring ice crystal linear and mass growth rates over a wide range of conditions, thus filling gaps in knowledge imposed by difficulties of growing ice crystals in the laboratory. Although wave clouds have not been used for growth rate studies, measurements could build upon such observations drawn from earlier laboratory studies.

b. Laboratory growth rate studies

What are the main findings from the laboratory growth rate studies, and can wave cloud observations be used to supplement them? Ryan et al. (1976, hereafter RWS76) measured the linear and mass growth rates of ice particles in free fall growing by vapor diffusion at temperatures from −3° to −21°C and at water-saturated conditions over periods from 50 to 150 s at a pressure of 1000 hPa. Takahashi et al. (1991, hereafter T91), building on laboratory measurements by Takahashi and Fukuta (1988), measured the growth of ice particles freely suspended in a vertical wind tunnel at 10 temperatures from −4° to −22°C over periods of 3–30 min at water saturation. Particles grew by diffusion and accretion, with a mean droplet diameter of about 8 μm. Atmospheric pressure during growth was 1010 hPa.

The RWS76 and T91 studies produced similar results, with the sizes that grew in the T91 studies being much larger because of their larger growth times. Growth along the *c* axis—needles and columns—predominated at temperatures between about −3° and −9°C (Figs. 1a,d). Growth along the *a* axis—plates through dendritic crystals—predominated at temperatures from −9° to −20°C. The peak linear growth rates on the order of several to 10 μm s^{-1} occurred at a temperature near −15°C (Figs. 1b,e), where the ratio of the *a*- to *c*-axis growth was particularly large (Figs. 1a,d); a secondary peak in the linear growth rate occurred near −5°C. RWS76 found linear growth rates to be somewhat higher after 100 s than before (Fig. 1b), presumably where ventilation effects become appreciable; this change in the growth rates was not notable in the T91 data (Fig. 1e). RWS76 and T91 cast the ice mass density of the crystals in terms of the bulk density, defined as the particle mass divided by its volume ρ_b. We extend the definition of their densities to an effective density ρ_e, which is the mass divided by the volume of a sphere of the maximum dimension of the particle. Hollows at the ends of columnar crystals and open growth of dendritic crystals lead to relatively low ice bulk densities near −5° and −15°C (Figs. 1c,f). Mean values of ρ_b are about 0.4–0.7 g cm^{-3}, whereas values of ρ_e are an order of magnitude smaller.

BH04 and BH09 measured ice linear and mass growth rates near water saturation at temperatures from −20° to −40°C (and below) and at atmospheric pressures that are realistic for those temperatures, from particles supported on filaments. Particle types were characterized by platelike polycrystalline shapes (sp, Fig. 2a); large, thin, overlapping skeletal and sector-like plates (pla); and columns (col). These growth rates decreased approximately exponentially with temperature below −20°C (Figs. 2a,b), with linear growth rates still near 1 μm s^{-1} noted at −20°C (Fig. 2a). Linear growth rates were fastest for the spatial particles, with lower rates for the plates and columns; factor of 2 differences between habits are noted. Bulk densities are relatively low, with little difference among habits but with a tendency for lower densities as temperatures increased (Fig. 2c).

Westbrook et al. (2008) calculated that the linear and mass growth rates derived from theory for freely growing ice crystals were significantly greater than those measured by BH04 for suspended crystals, arguing that the vapor field may have been strongly affected by neighboring crystals, restricting the vapor supply. An alternative explanation is that the growth of complex, 3D-type polycrystals responded to complex vapor fields in their vicinity relative to those found for pristine ice.

Riming should enhance crystal linear and mass growth rates in supercooled cloud. Drawing upon the laboratory growth studies of T91 and Takahashi and Fukuta (1988), Fig. 3 compares ice linear and mass crystal growth by diffusion alone to growth in supercooled cloud with a liquid water content of about 0.1 g m^{-3} and a mean droplet diameter of 8 μm. The data are segregated into three temperature ranges that exhibit characteristic crystal habits, and those crystals that did rime in the liquid cloud growth experiments are identified. Note that the atmospheric pressure during growth is slightly different in the two studies: 1000 versus 800 hPa, respectively, and for the rimed experiments masses were measured for all crystals but diameter was not always obtained. Linear growth rates are fastest in the −12° to −18°C temperature range, not surprisingly, and remain at nearly 1 μm s^{-1} throughout the growth periods, whereas for the lower and higher temperature ranges linear growth rates slow with size and time (left panels). Mass growth rates continue to increase with time throughout the growth periods (right panels). Although there is considerable scatter in the results, growth via diffusion and accretion does not markedly increase the sizes over diffusion alone, at least for the conditions used in the T91 study. The sample size was small, though. The slope of the rimed crystal mass versus

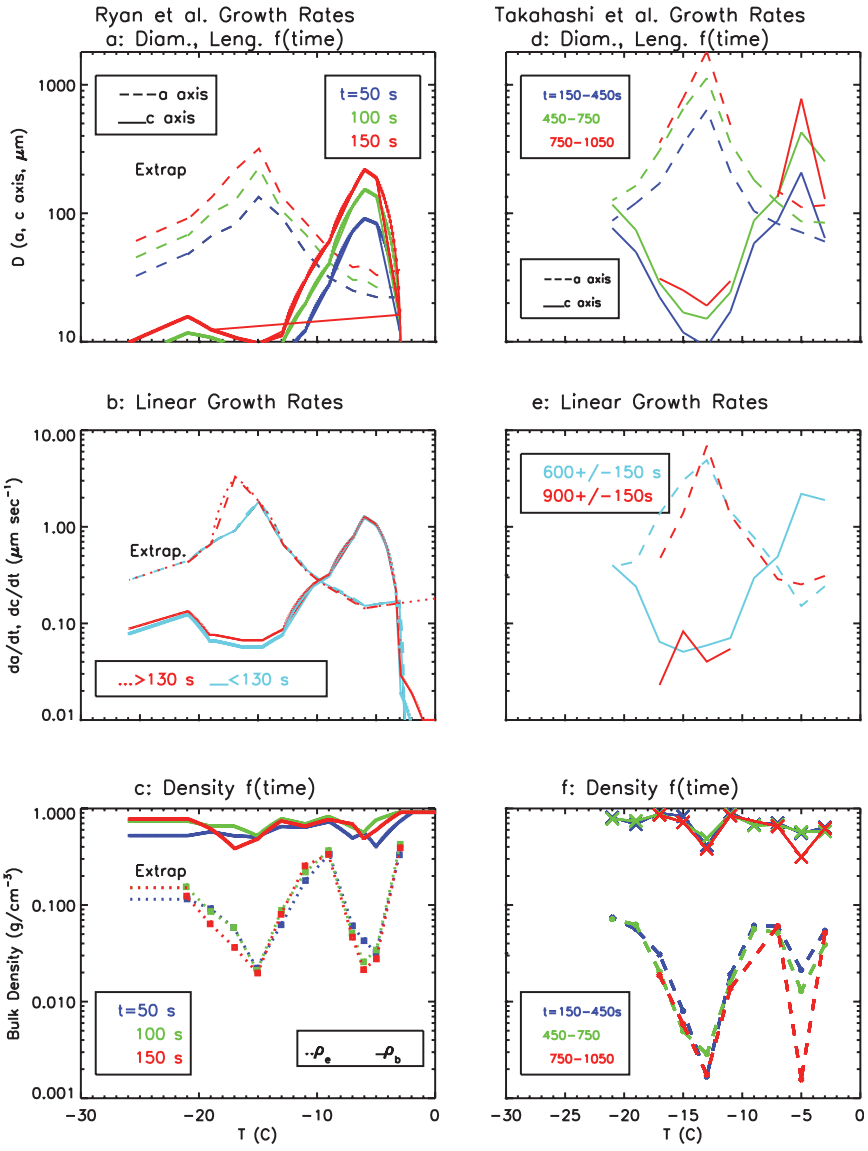

FIG. 1. Laboratory growth of pristine ice particles as a function of temperature at water saturation, adapted from the studies of (left) RWS76 and (right) T91. (a),(d) Increase in *a*- and *c*-axis dimensions with time. (b),(e) Linear growth rates. (c),(f) Mean bulk and effective densities.

time appears to be higher than that for the unrimed crystals, suggesting enhanced mass growth rates. For reference, arrows in Fig. 3 point to crystal riming threshold sizes and 25% crystal areal coverage for the relevant crystal types from the Reinking (1979) study. Crystals fell to the ground and riming was identified using a microscope. The threshold size for riming in the experiments is similar to these ground-based observations. Given the sizes where 25% of the crystal area is covered by rime, it is not surprising that the laboratory measurements do not show stronger influences from riming.

To summarize, the RWS76 and T91 studies measured ice crystal growth rates at temperatures from about −3° to −23°C and at water saturated conditions where habits were dominated by pristine, single hexagonal ice crystals, except near the lower end of that temperature range. The particles were freely falling, and enhanced growth through ventilation could have been significant at the larger sizes considered. Riming onset occurs at sizes of 100–300 μm, depending on the habit, but for sizes up to 400 μm or above the riming onset does not appear to have a dramatic effect on linear and mass growth rates.

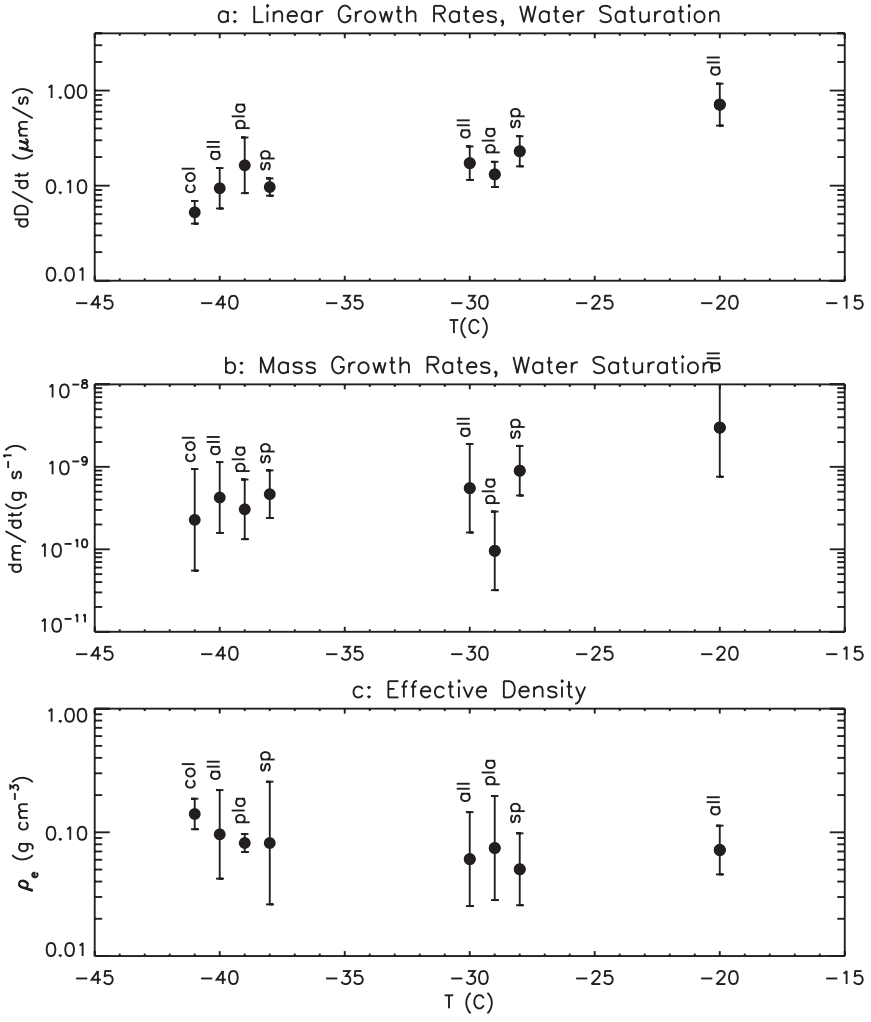

FIG. 2. As in Fig. 1, growth rates derived from BH04 and BH09, at conditions within a few percent of water saturation and at pressures that decrease with temperature, for particles generally 300 μm and below. The data are shown for all habits combined (all) and partitioned according to whether they were polycrystals (sp), plates (pla), or columns (col): (a) linear growth rates, (b) mass growth rates, and (c) effective density.

The laboratory experiments provide a relatively complete depiction of how pristine, hexagonal ice particles and rimed crystals develop during their early growth over this temperature range, with the exception that the pressure levels for growth were at 800–1000 hPa, so we do not see the more rapid growth that occurs at pressure levels representative of ICE-L conditions.

Although some morphological differences can be expected when growth occurs at sub-water-saturated conditions, growth rate calculations can be used as a first approximation to extend those results to lower pressures and ice supersaturations. BH04 grew ice crystals that were supported on filaments and measured their growth rates with temperature and with pressures that correspond approximately to the ambient temperatures studied. Considering their results for $-40° < T < -20°$C, simple hexagonal crystal shapes and polycrystals are observed at a given temperature, with corresponding habit-dependent linear growth rates. Complex crystal shapes of the types generated in the BH04 study were observed at comparable temperatures in the wave clouds sampled by Baker and Lawson (2006), adding realism to the laboratory measurements. Because the BH04 measurements focused on particles that were generally smaller than 300 μm in maximum dimension where ventilation enhancements are considered to be small, growth on the supporting filaments would not likely have had a significant impact on the growth rates over the particle size range they studied. However, given the discrepancy between the observations and theory and perhaps

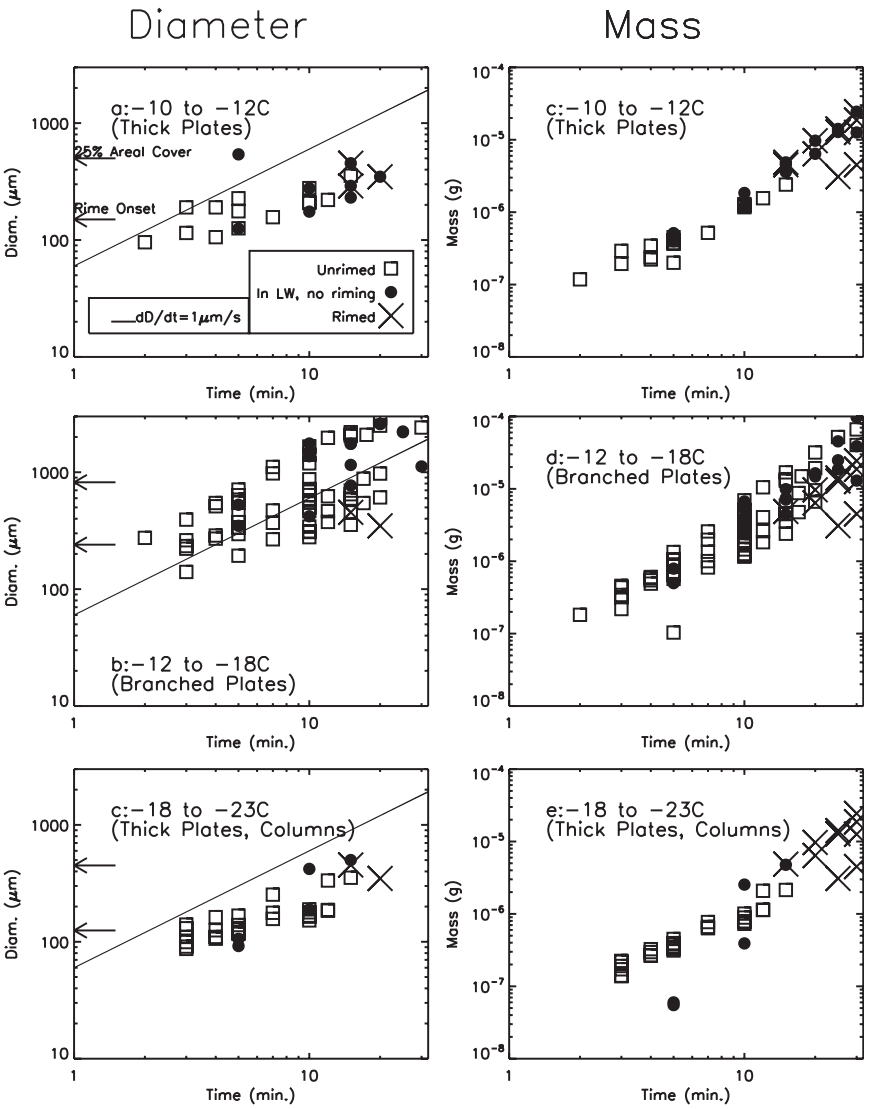

FIG. 3. Comparison of diffusion-grown crystals to those that grew in an environment with an LWC of about 0.1 g m^{-3} in the laboratory experiments of T91 and Takahashi and Fukuta (1988). (left) Maximum dimension vs growth time. (right) Mass vs growth time: (top to bottom) thick plates, branched plates, and thick plates–columns. Data kindly provided by T. Takahashi.

effects due to the complex geometry of crystals that grow at temperatures below −20°C, there is clearly a need to estimate their growth rates at water saturation where complex crystals form; these conditions are relevant for particles initially developing in altocumulus and deep convective clouds.

Results from earlier laboratory studies can be augmented by growth rates derived from wave cloud observations because (a) the number of particles considered can be greatly increased; (b) limitations associated with the suspension of ice particles—filaments that restrict enhanced growth by ventilation, for example—are removed; and (c) ice nucleation is representative of the freezing process occurring in natural clouds, a potentially important factor that determines the initial ice particle size and resulting distribution of ice particle habits. Drawing upon the ICE-L measurements through orographic wave clouds at multiple levels with numerous particle probes covering a wide range of sizes, the objectives of this study are threefold: 1) to evaluate new airborne instruments that can more precisely provide data relevant to ice crystal linear and mass growth rate studies, 2) to expand upon the laboratory measurements of ice crystal growth rates for single ice particles via diffusion at temperatures between

−20° and −40°C, and 3) to evaluate whether ice nucleation is nearly instantaneous or occurs over a period of time after water saturation is reached.

In section 2, we discuss the ICE-L dataset and in section 3 present the observations of ice crystal growth rates. Conclusions are drawn in section 4.

2. ICE-L data and instrument evaluation

a. Data collection

The data reported here were collected during the Ice in Clouds Experiment—Layer Clouds (http://www.eol.ucar.edu/projects/ice-l/). In situ and remote sensing data were collected from the National Science Foundation (NSF) C-130 aircraft operated by the National Center for Atmospheric Research (NCAR). The C-130 was equipped with a full complement of spectrometers to measure aerosol, cloud droplet, and ice size distributions. Two scattering probes were used to measure the PSD in sizes from 1 to 50 μm: an open-path cloud droplet probe [CDP; 3–43 μm, Droplet Measurement Technologies (DMT)] and a forward-scattering spectrometer probe [FSSP; 0.8–50 μm, manufactured by Particle Measuring Systems (PMS) with electronic updates by DMT]. The PSD and the particle cross-sectional areas for particle diameters 50–6000 μm were measured by probes that provided two-dimensional images of the particles: a cloud particle imager [CPI; ~(20–600) μm, Stratton Park Engineering Co. (SPEC)], a "fast" two-dimensional cloud (2DC) (50–1500 μm, PMS updated by NCAR), a 2DS (stereo, 20–1500 μm, SPEC), a gray scale CIP, part of a cloud and aerosol spectrometer (20–1500 μm, DMT), and a 2DP (200–6400 μm, PMS). Redundant capabilities, size overlap, and different probe designs reduced known problems and uncertainties in the measurements of small particles. Concentrations of ice nuclei (DeMott et al. 2003) and condensation nuclei were also measured (Part II). The presence of supercooled water was estimated from a Rosemount Icing Probe (RICE), and the amount from the RICE using the technique developed by Mazin et al. (2001).

The total amount of condensed water (CWC; the sum of the liquid and ice) was measured by a counterflow virtual impactor (CVI; Twohy et al. 1997). The CVI LWC derived from a well-calibrated near-infrared humidity sensor has been shown to be accurate to within about 15%, when inlet mounting location is not a factor (Twohy et al. 2003; Davis et al. 2007). Potential flow modeling (see King 1984; Norment 1988, and references therein) suggests that at the CVI's mounting location on the C-130, 38 cm from the fuselage, there may be concentration enhancements for particles with small aerodynamic diameters and a shadow zone for larger particles. Because of this large uncertainty, which is exacerbated in ice clouds due to uncertainties in ice aerodynamic diameters, CVI CWCs are not used quantitatively in our analysis below.

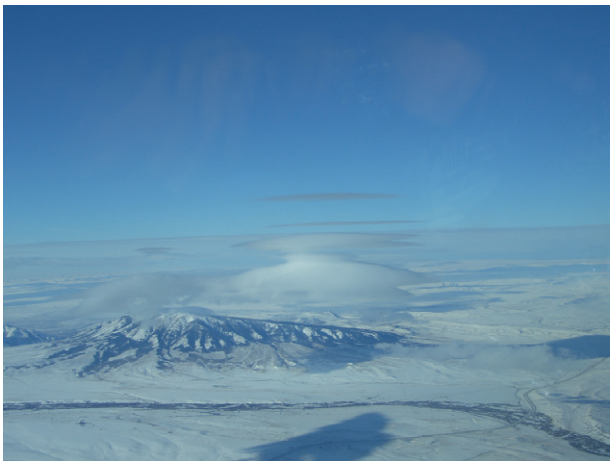

FIG. 4. Wave cloud sampled over Elk Mountain, WY, on 13 Dec 2007 (RF11). The time is 1642 UTC, temperature at the aircraft level is −23°C, and the altitude is 5.5 km. The picture is looking toward the west, approximately into the wind.

A 3.2-mm upward- and downward-viewing Doppler cloud radar (WCR) and an upward-viewing two-wavelength polarization lidar (WCL), operated by the University of Wyoming, provided remote sensing data. Relative humidity was measured with a Maycomm Instruments tunable diode laser hygrometer (TDL) and a Buck Research chilled mirror hygrometer. Research-grade instruments measured the temperature, pressure, and air vertical motions (derived from a combination of measurements from inertial reference, GPS, and radome gust systems).

Wave clouds were sampled on nine days in 2007. A typical cloud is shown in the photograph of Fig. 4. Two regions of wave clouds were sampled on each of the days except for RF01 and RF02. Upon arriving at the cloud to be studied (e.g., Figs. 4 and 5), transects were conducted along the wind direction from the leading to trailing edges of the wave clouds, alternating with reverse headings, with additional legs extending upwind and below cloud base to characterize the thermodynamics, vertical velocity, and condensate and aerosol particle size distributions, if present, in the pre-cloud environment (e.g., Figs. 5 and 6). The average number of penetrations per cloud was nine. For each flight leg, upwind and trailing edges of the liquid wave cloud layer were identified and a mean layer wind direction and speed derived. Horizontal wind speeds and directions did not vary by more than a few meters per second through the cloud layers (e.g., Fig. 6). Using the

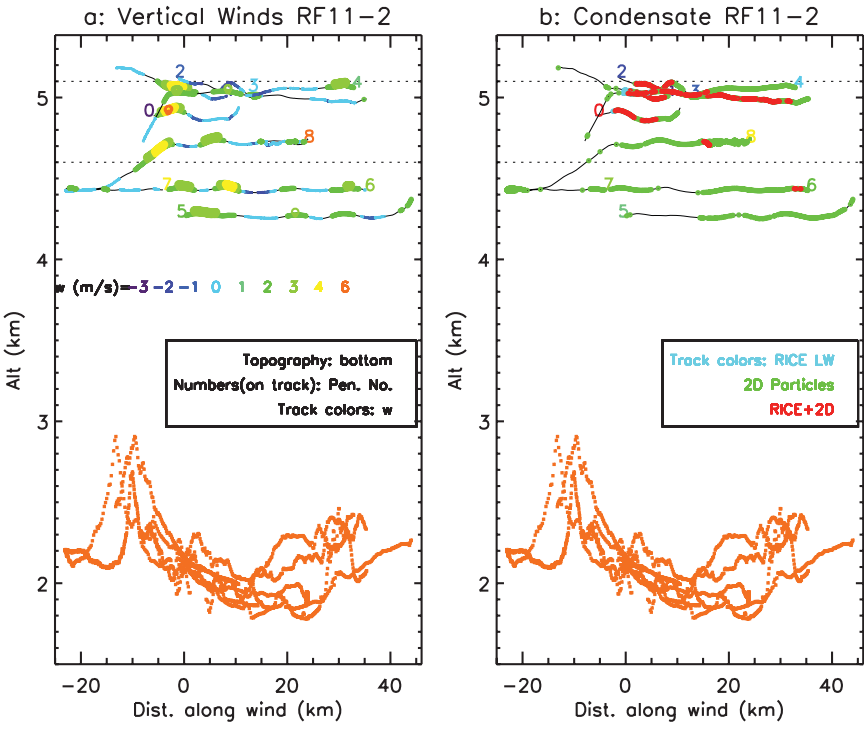

FIG. 5. Structure of cloud measured during penetrations on 13 Dec 2007 (RF11), over Elk Mountain, WY. Topography below the aircraft as derived from the Geographic Information System (GIS) database is shown below 3 km. Penetration number is shown at the beginning of each penetration. Abscissa is distance in rotated coordinate system as discussed in text. (a) Vertical velocities, color coded, with scale shown across 3.8-km level. (b) Condensate (cloud) locations, color coded according to where liquid water was observed with a Rosemount Icing Probe and where ice particles were observed with a 2DC probe.

mean wind direction and speed and the liquid cloud edge as a marker, distance and advection time along the wave cloud streamlines were defined by projecting the flight track onto the direction of the horizontal wind for each flight leg.

Sampling through the vertical cloud depth allowed us to characterize the temperature and wind structure through the cloud layers. The average depth of the liquid cloud layer sampled (generally from cloud bottom to top) was 0.96 km. For a given pressure level, the warmest temperatures were generally noted where liquid water and mixed-phase conditions (liquid from the RICE plus ice as observed from 2DC probe particle data) occurred in the upward moving parts of the cloud; the coolest temperatures were noted in the out-of-cloud (upwind of the leading cloud edge) environment (Fig. 6). Lapse rates were below the moist adiabatic rates, consistent with wave cloud thermodynamics that places them in a stable layer (Fig. 6).

In-cloud temperatures T for the 139 flight legs spanned the range $-10° < T < -40°$C (Fig. 7a). The mean difference between the aircraft and wind direction, by penetration, spanned a wide range (Fig. 7b). In the analysis that follows, we have used penetrations where the absolute value of this difference was less than 30° (horizontal lines, Fig. 7b). Data from the penetrations that sampled the leading and trailing cloud edges and were within 30° of or against the wind direction were generally where temperatures ranged from −20° to −33°C (Fig. 7a).

b. Instrument evaluation

Accurate measurements of the 1) LWC and IWC, respectively, 2) relative humidity, and 3) concentrations of ice particles are necessary for our study.

1) LIQUID AND ICE WATER CONTENT

We have evaluated the accuracy of the various probes used to derive the presence and amount of liquid water for ICE-L by using the King Probe measurements as a standard, with an approximate accuracy of better than ±15% (Strapp et al. 2003). The King probe has a detection threshold of about 0.05 g m^{-3}, below which noise and drift effects from changing airspeed mask the LWC signal. In high ice water content regions (not present in

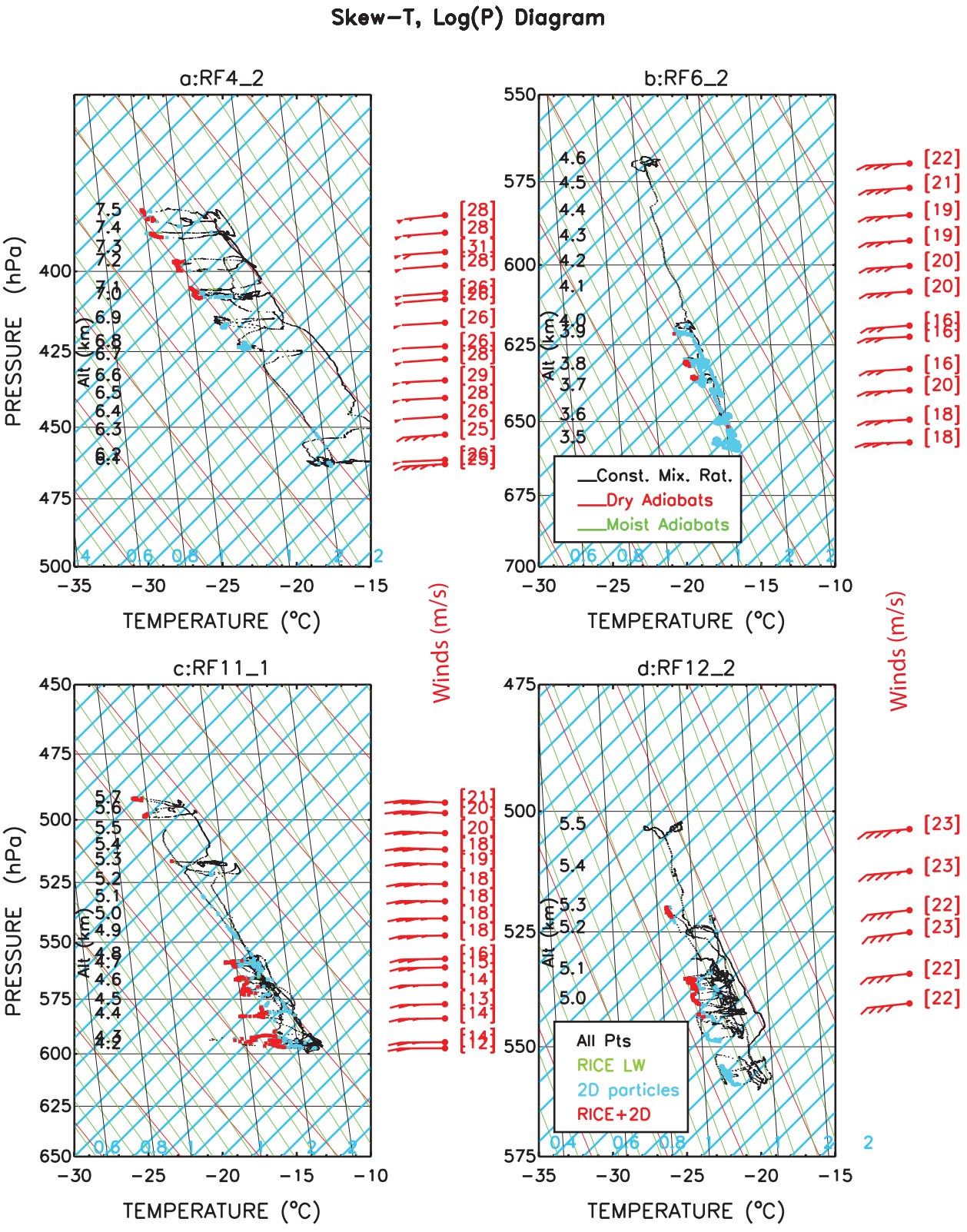

FIG. 6. Soundings derived from measurements during penetrations by the C-130 through four wave cloud layers. The solid nearly vertical lines represent constant water vapor mixing ratios. Dry adiabats have steeper sloping lines than moist adiabats. Locations where liquid water as detected by the Rosemount Icing Probe (RICE), ice particles by the 2DC particle imaging probes, and where both were observed simultaneously, are indicated. The wind speeds and directions are plotted and listed in red. Data from times designated as wave cloud penetrations are shown.

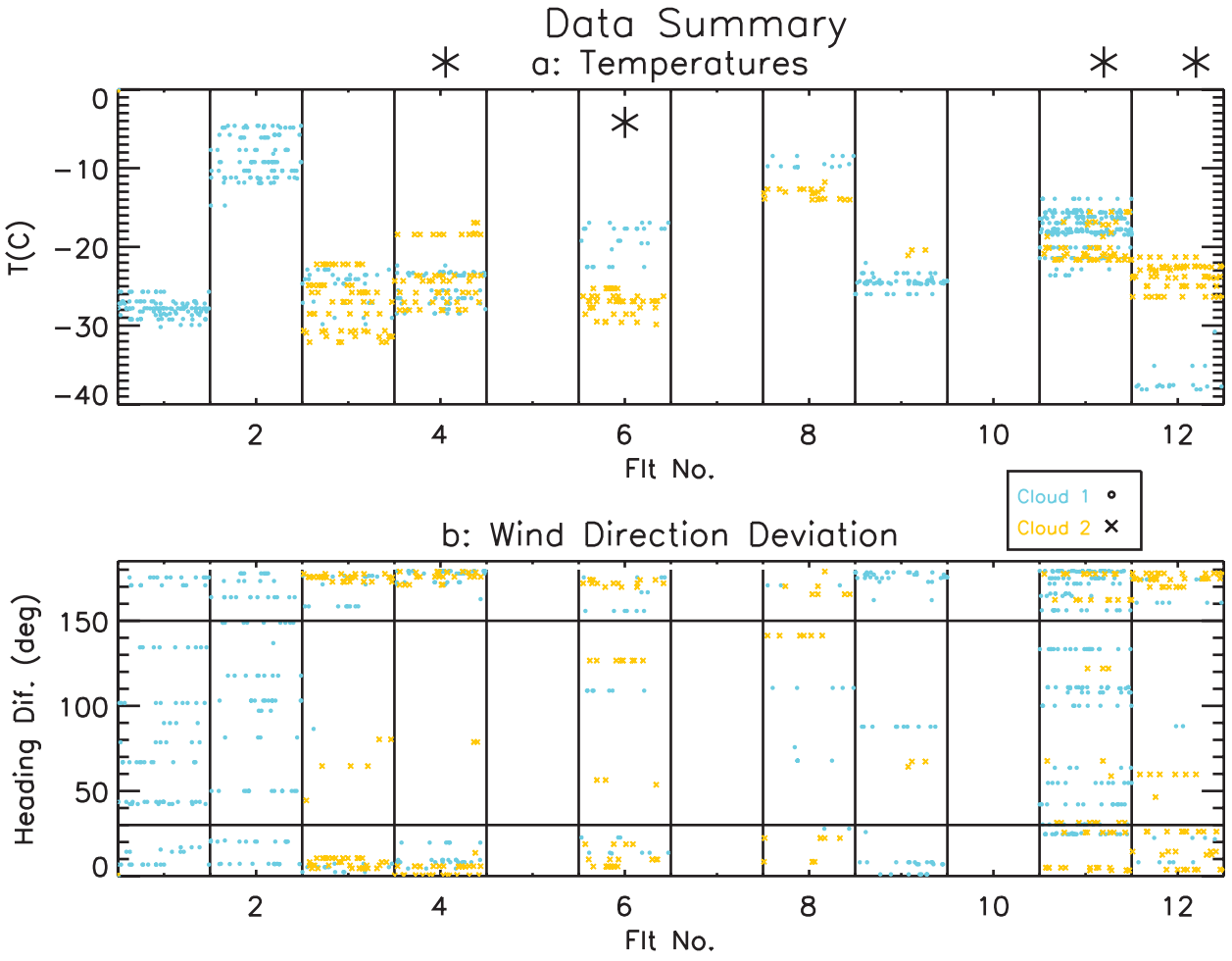

FIG. 7. Summary showing (a) cloud mean penetration temperatures and (b) penetration mean difference between the aircraft heading and the layer-mean wind direction. In (b), horizontal bars show where the absolute value of the difference is 30°; data above the top line and below the bottom one are used in the analysis. Data from flights 5, 7, and 10 were not shown; these were not wave clouds. In (a), large asterisks show where the greatest number of penetrations were nearly along or against the wind direction.

ICE-L), the King Probe responds to ice, raising these detection thresholds and accuracies. The probes' collection efficiency reaches nearly unity for droplets of 10-μm diameter and, although not a problem for ICE-L, diminishes for droplets approaching 100-μm diameter and above because of splashing.

We evaluate those situations where there are few to no particles detected by the 2DC probe. For these situations, the CVI probe should measure the LWC in droplets above a ''cut'' (minimum detectable) size of about 9-μm diameter. The CVI's detection threshold is about 0.01 g m^{-3} for droplets above the cut size. The CVI LWC's are systematically about 20% below the King Probe values (Fig. 8a), with no strong dependence on the LWC. Much of the scatter observed in Fig. 8a can be attributed to artifacts produced by hysteresis (time lag) noted in the plumbing of the CVI when entering and exiting cloud. Using data from the CDP probe, Fig. 8b lists the fraction of the CDP LWC that falls in diameters 9 μm and below where the CVI cut size was set for ICE-L. If the CDP sizing is accurate or overestimated as suggested below, only a small percentage of the LWC is contained within sizes below the CVI's aerodynamic (for unit density spheres) cut size. The LWCs derived from the CDP are about 40% higher than those from the King probe (Fig. 8b and the LWCs from the FSSP appear to be even more overestimated (Fig. 8c). The FSSP concentrations are about 50% larger than those for the CDP, accounting for the CDP–FSSP difference. The LWCs derived from the RICE probe closely track the King Probe data, although with a small overestimate (Fig. 8d). Some of the scatter noted in Fig. 8d is due to the difficulty of completely eliminating fluctuations in the icing probe's signal voltage due to C-130 airspeed fluctuations.

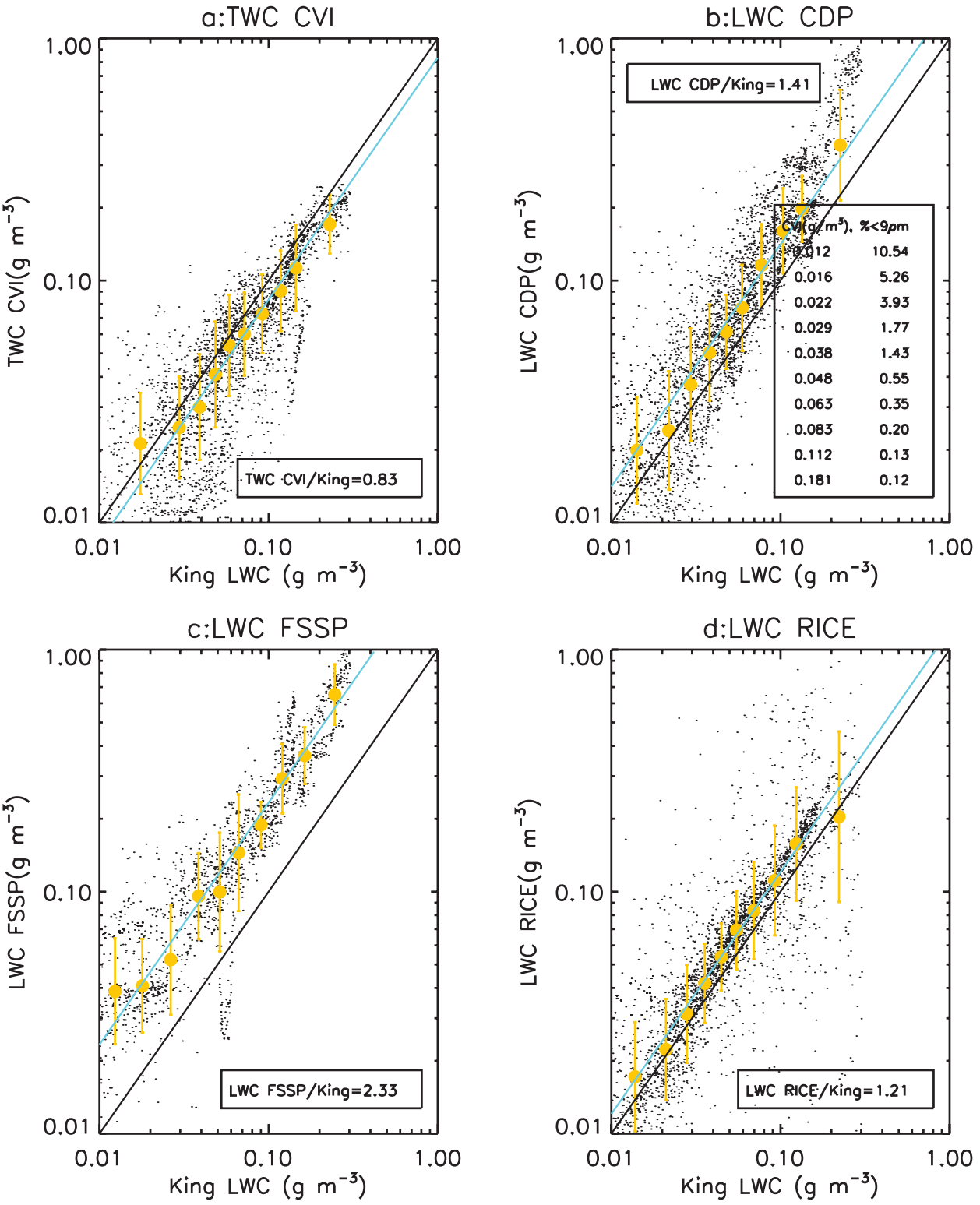

FIG. 8. Evaluation of liquid water measurements, where King LWC is compared against (a) CVI condensed water content (CWC) and (b)–(d) LWCs derived from the size distributions measured by the (b) CDP and (c) FSSP probes, and (d) the rate of change of voltage measured by the Rosemount icing probe. Periods are chosen where the IWC in 2DC+2DP probe sizes is greater than 0.01 g m^{-3}. In all panels, the 1:1 (black) line and the median values of the variable on the ordinate as a function of the King LWC (yellow) are plotted and the median ratio of the LWC from each probe to the King LWC is listed, and in (b) the legend on the right lists the median fraction of the CDP liquid water content below the CVI cut size (%) as a function of the CVI CWC. Each plotted data point is a 1-s value from 1 of the 139 penetrations through wave clouds.

In summary, for liquid regions, the CVI underestimated the LWC by about 20%, the CDP overestimated it by about 50%, and the FSSP overestimated it by more than a factor of 2. The presence and amount of RICE LW closely mirror the King Probe LWCs.

2) RELATIVE HUMIDITY

Outside of clouds, the relative humidity was derived from the ratio of the measured mixing ratio to the mixing ratio at saturation at the ambient temperature from measurements taken by a Buck research cryogenic hygrometer and a Maycomm TDL hygrometer. The TDL measurements were corrected for an apparent temperature offset by using liquid water regions from the RICE probe to signify an RH of about 100%. The RH measurements from the TDL are a few percent higher than for the Buck instrument; where liquid water is detected from the RICE probe, the measurements from both probes now agree well and are within a few percent of 100% RH (Fig. 9a). This result is further examined in Fig. 9b, where it is noted that when RICE LW is detected, the RH measurements are within a few percent of water saturation. For the entire dataset, where RICE LW is detected and drop concentrations from the CDP are greater than 10 cm^{-3}, the median value of RH from the TDL hygrometer is 100.3% and from the cryogenic hygrometer is 100.6%. Some of the scatter in Fig. 9 is due to different temporal responses of these instruments: in relative terms, the TDL is fast, RICE intermediate, and Buck slow.

3) PARTICLE PROBE MEASUREMENTS

There are several issues of uncertainty in concentration measurements from the particle probes. Probe sample volumes for the small particle probes at 1-Hz temporal resolution are used in this study and require a minimum detectable concentration of about 10 L^{-1}. For the imaging probes, the sample volume at small sizes is only approximately known. Furthermore, shattering of small ice has the potential to increase the concentrations from these probes as an artifact. Although corrections for shattering were conducted as in Field et al. (2006), such instances were negligible for the ICE-L wave cloud observations.

The 2DS probe has a nominal detection size of about 20 μm whereas the fast 2DC detects particles above about 25 μm. The 2DS probe was operating on the C-130 only for the first four flights. Measurements from the 2DS probe, which were processed to reduce shattering, were used to evaluate data collected by other particle probes during ICE-L.

Figure 10 compares 2DS concentrations to those measured by other ICE-L probes in sizes from 30 to 50 μm in diameter, partitioned according to whether in liquid or ice (LWC < 0.01 g m^{-3}) as derived from the RICE probe. The FSSP must be oversizing and/or responding to shattering because the concentrations are much higher than the 2DS probe (Fig. 10). The CDP concentrations measured above its nominal concentration detection threshold are reasonable (Fig. 10b). Concentrations derived from the CPI, using the procedure developed by Connolly et al. (2007), show little agreement with the 2DS measurements (Fig. 10c). Using just one size bin of the fast 2DC probe—centered on 50 μm, the smallest size that could be reliable—a good correlation with the 2DS is noted, but the concentrations are evidently too high, presumably because particles are sized too small and hence the sample volume is too large.

Figure 11 compares concentrations measured by the 2DS and 2DC in approximately the same size ranges as a means of inferring how well the 2DC, with a larger resolution and size detection threshold, can sample small particles. Size is defined as the maximum particle diameter as found by fitting a circle around each 2DC and 2DP probe image. The 2DC concentrations are likely overestimated in its first size bin centered on 50 μm (25–75-μm bin), as the concentrations in the 40–80-μm range sampled by the 2DS are considerably lower (Figs. 11a,b). The 2DC concentrations are overestimated presumably because of an underestimated particle size, because the corrected sample volume is proportional to square of the particle diameter. Above 100 μm, concentrations between the two probes agree well, although at low concentrations they differ, presumably because of differences in the way that the sample volume is derived. This comparison suggests that 1) the concentrations from the 2DC probe above a maximum dimension of 100 μm are likely to be accurate, and 2) the scattering probes, sampling at a rate of 1 Hz, cannot detect ice concentrations below 10 L^{-1} and are of limited value in the analysis.

3. Results

This section addresses the two primary objectives of this study: an evaluation of ice crystal linear and mass growth rates relative to those predicted by theory and observed in the laboratory; and, based on those results, an explanation for why the total ice concentration increases with time downwind of the leading cloud edge. Our interest is in evaluating the rate of ice nucleation and growth as they affect the breadth of the ice particle size distribution that develops in wave clouds.

Our attention is directed to temperatures of -20°C and below, where most of the ICE-L penetrations were made. In laboratory studies, plate habit crystals with etched-out regions on their sides (skeletal) were

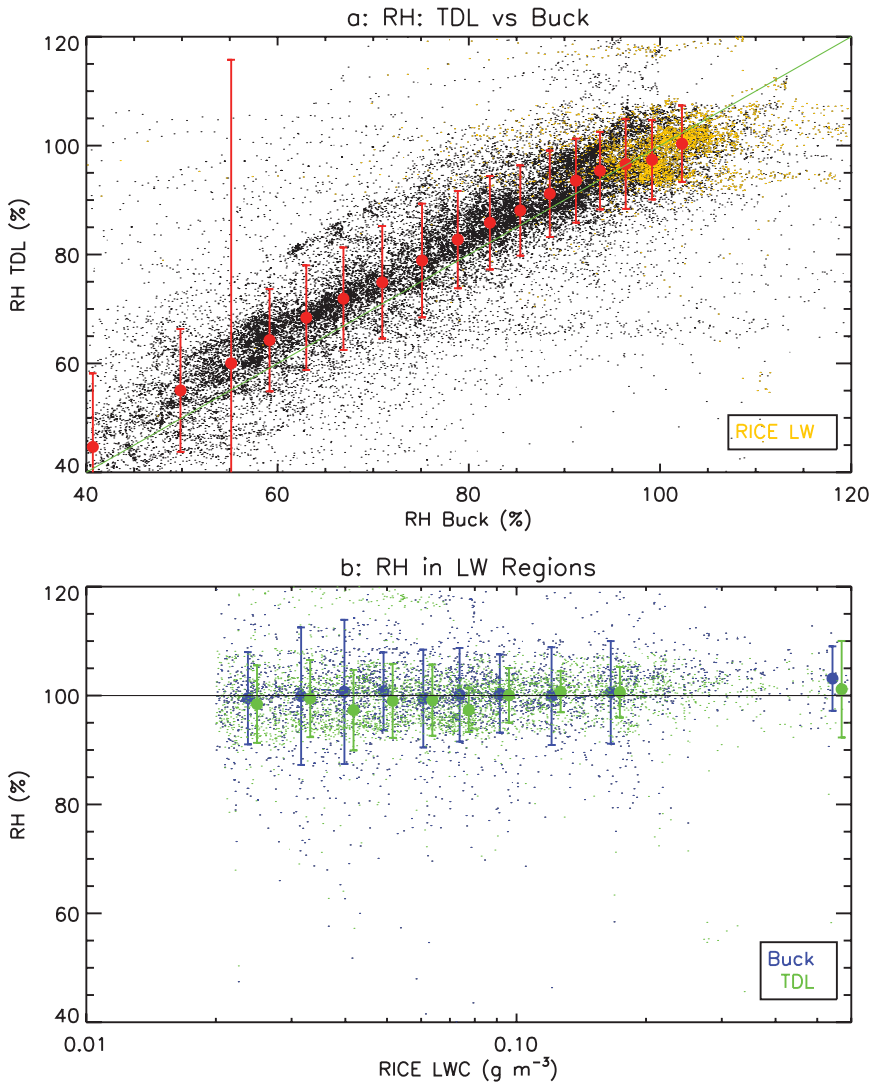

FIG. 9. Evaluation of RH measurements from ICE-L. (a) Comparison of Buck and TDL hygrometer measurements. (b) Measured RH as a function of LWC derived from RICE probe measurements. Colored points and vertical bars show median values along the ordinate as a function of the value along the abscissa. Each point is a 1-s value.

observed just below −20°C (RWS76; T91), changing to hollow columns near −23°C (T91). BH04 characterized particles at temperatures below −20°C as plate-like polycrystals such as side planes, plate rosettes (spatially branched rosettes of side planes, scrolls, and other polycrystalline habits found in BH04), overlapping parallel plates, and irregular assemblages of plates, with a low frequency of single plates (often large, thin, and skeletal, or sector-like), and very low frequencies of short columns. We find similar results: ice particle habits comprise predominantly polycrystalline shapes, with few regular hexagonal shapes observed (Fig. 12). The exception was for RF12 (second cloud), with as much as 50% columns when cloud-base and cloud-top temperatures were −23° and −26°C, respectively, and ice particles neither were carried into the cloud nor fell in from above. Side planes of the type observed by BH04 and BH09—structures that develop from the center of rosettes, and from the surfaces of particles of other types as suggested by Baker and Lawson (2006)—are observed. Given that the shapes of the ice crystals are similar to those studied by BH04, the effective densities should be similar to those observed by those authors—about 0.1 g cm^{-3}. Although we are unable to directly derive values for ρ_e within the parts of the clouds where nucleation is occurring for instrument-related reasons discussed

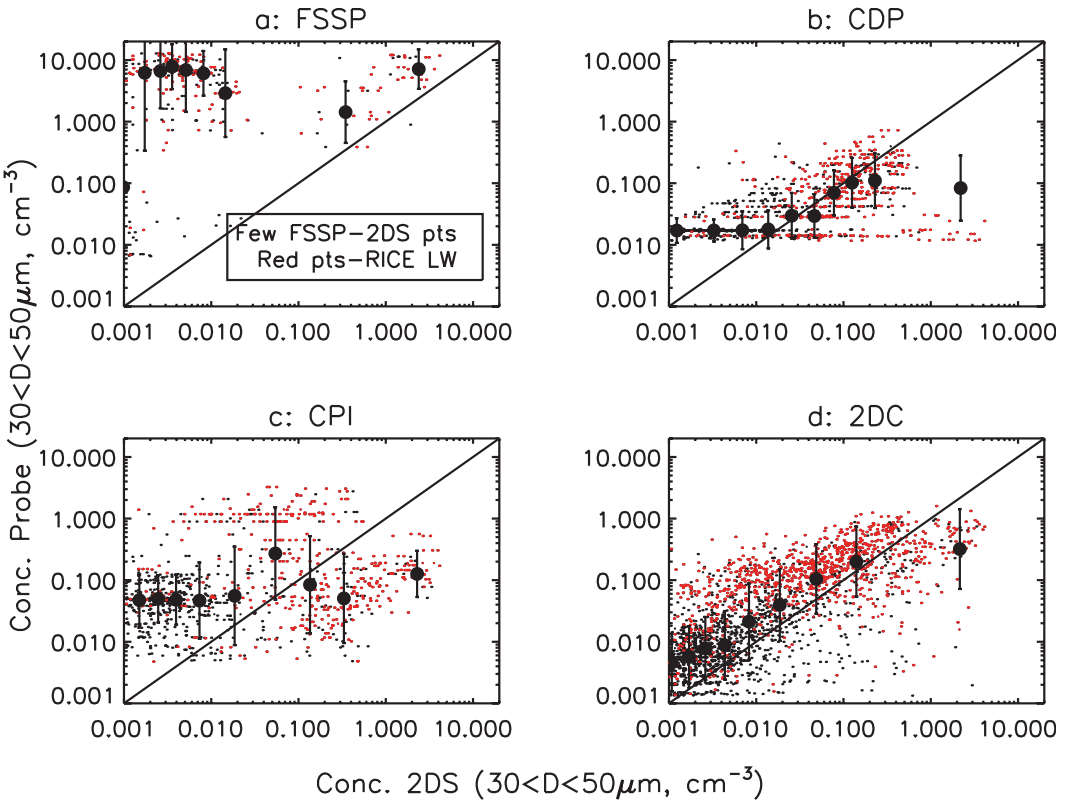

FIG. 10. Comparison of concentration measurements from the 2DS in the size (maximum dimension) range 30–50 μm during ICE-L, to those derived in the same size range from the (a) FSSP, (b) CDP, (c) CPI, and (d) 2DC, but for one size bin centered at 50 μm. Median values per concentration interval are indicated. Each point is a 1-s average from ''designated'' wave cloud penetrations from flights RF01-RF04. Red points denote where liquid water is measured.

later, effective densities in the ice-dominated regions where we could derive them are comparable to those of BH04.

Ice crystal growth rates were derived along 13 of the 139 designated wave cloud penetrations. This subset of the data was chosen because the penetrations were aligned within $\pm 30°$ along or against the wind direction, and the aircraft passed through the upwind edge of the cloud, with no evidence from the remote sensing observations of particles entering into the cloud from upwind and without significant fallout of ice particles from above or entering from below. Temperatures of the 850 1-s data points during this subset of penetrations spanned the range $-21°$ to $-32°$C, with peak updrafts reaching 3 m s^{-1}. The ambient relative humidity was usually within a few percent of water saturation (median value of 100.3% for the TDL; 100.6% for the cryogenic hygrometer), although some of the RH measurements are obviously in error as ascertained by the presence or absence of liquid water. Time lag caused some obvious errors in the cryogenic hygrometer measurements (Fig. 13e).

Droplet concentrations usually increased abruptly at the leading cloud edge, although there was occasional structure noted near the edge (Fig. 13). For reference, 1 s of aircraft time for the subset of penetrations corresponds to median and mean parcel transit times of 6.3 and 5.8 s, respectively. During the ~6 s of particle growth time (corresponding to about 1 s of aircraft time) between data points, a parcel in an updraft would have moved vertically less than 12 m; therefore, over 1-s intervals of aircraft time, the C-130 nearly followed the air parcel streamlines.

Some period of time was required downwind of the leading cloud edge before the 2DC probe first registered particles (Figs. 13a,b). (For continuity throughout the various flights, the 2DC rather than 2DS data were used.) Thereafter, concentrations increased downwind. Often the ice region was vertically thin; thus, in the descending branch of the wave—we call it the ''ice tail''—the ice was often carried in downdrafts to below the aircraft level (Fig. 13e; see also Fig. 15). Consistency was usually noted among the RH measurements, droplet concentrations, and vertical velocities, with the previously noted time

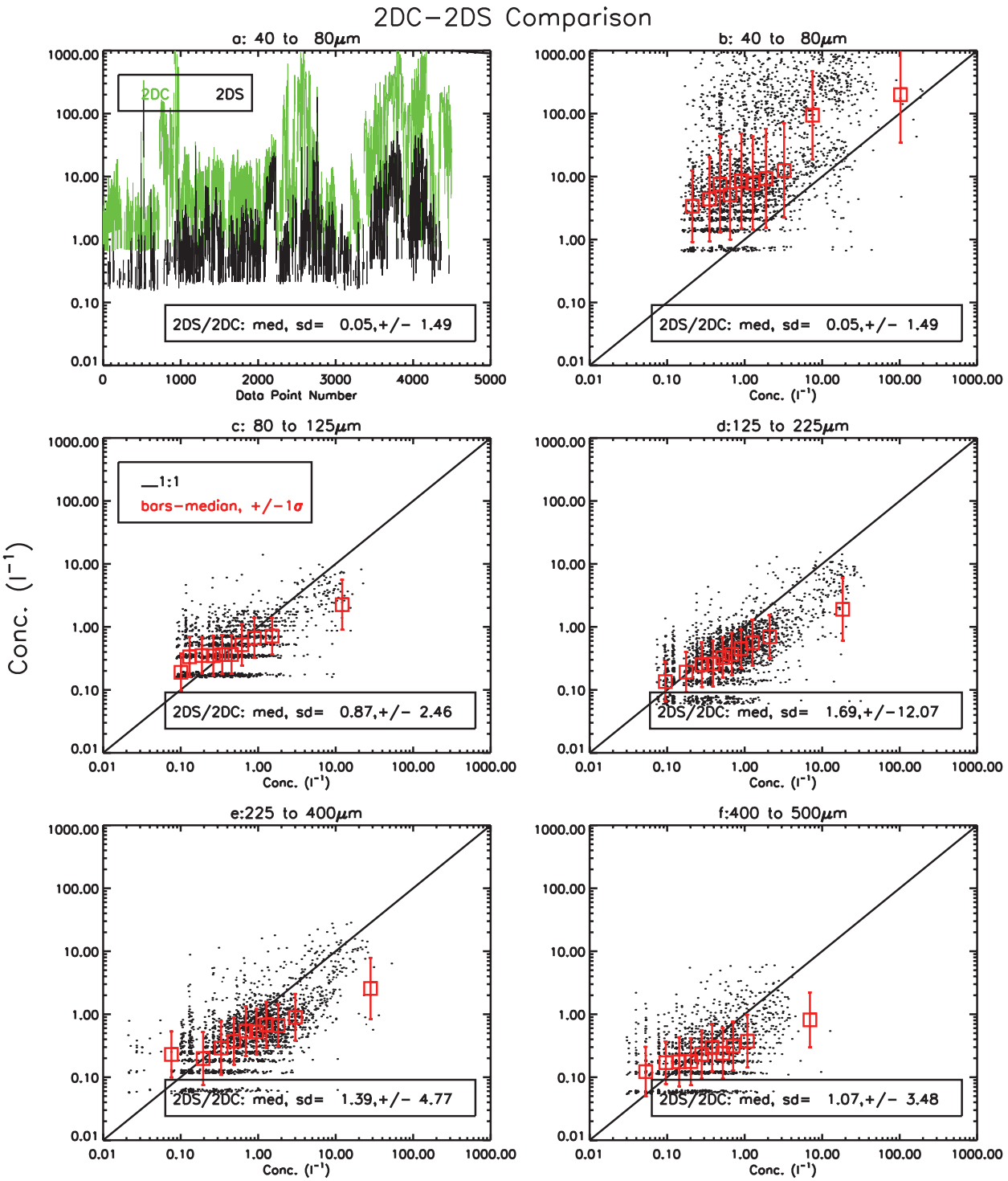

FIG. 11. Comparison of concentrations measured by the 2DC and 2DS probes for all 5-s average size distributions where data from both probes were obtained from designated wave cloud penetrations from RF1-RF4, (a) for the 40–80-μm size (maximum) range, plotted as a series of points, and (b)–(f) as scatterplots in five particle size (maximum) ranges, with median values of the ratio of 2DS/2DC concentration shown.

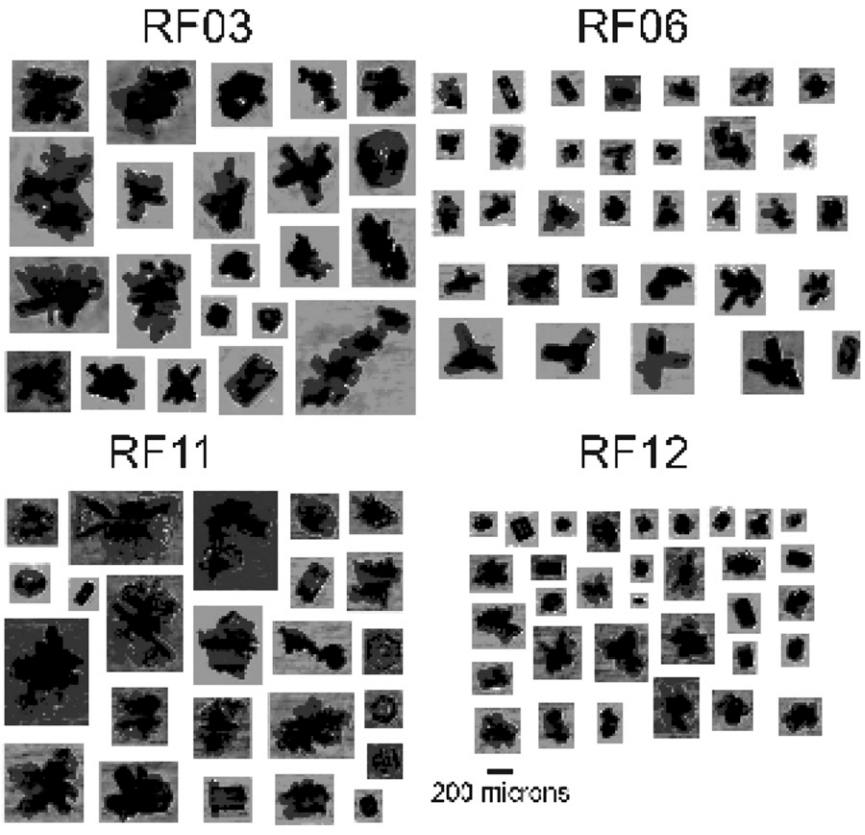

FIG. 12. Example images of ice particles sampled on four flights during ICE-L.

lag observed for the cryogenic hygrometer data (Figs. 13a,e). Note that the 2DC PSDs 100 μm and above are used in the analysis, except where noted, because of questions related to the measured concentrations and sizing of sub-100-μm particles.

a. Derived growth rates

1) LINEAR GROWTH RATES

Our most direct measurement of growth rates was from the change in particle size with time downwind of the leading cloud edge. For each 1 s of sampling by the 2DC probe during a penetration, we derived the cumulative distributions of the number concentration with size and of the ice water content with size, normalized by the total amounts, to find the median number and mass-weighted diameters D_n and D_m, respectively, and the maximum measured particle size $D_{\max}$ (Fig. 13b). The D_n and D_m values are derived from interpolation of these 1-s cumulative values using a boxcar smoothing method to mitigate possible errors due to the sample size.

Linear growth rates are derived from the change in the 1-s smoothed values of D_n, D_m, and $D_{\max}$ along the wind direction, in liquid water regions. By taking 1-s time increments, errors resulting from new nucleation, probe size detection thresholds, and crossing of streamlines are minimized. The time available for growth in those 1-s intervals is derived from the horizontal wind velocity, accounting for the difference in the C-130 heading and the wind direction and whether the penetration is along or against the wind. Linear growth rates (Fig. 14) are comparable to those derived at conditions of water saturation by BH04 (although no size dependence was found), yet are relatively large if compared to extrapolation of the RWS76 and T91 values to temperatures lower than observed in their experiments (see Fig. 1b). This is consistent with the higher vapor diffusivity present in the results of BH04 obtained at lower pressures than those used by RWS76 and T91, which should result in larger growth rates. The rates show a tendency to decrease with temperature, not unlike those measured by BH04 (Fig. 2a). We do not find any dependence of the linear growth rate on size in our data. Measurement accuracy in our dataset might have impeded the ability to detect size-dependent trends.

To examine further the linear growth rate estimates, we focus on one case, RF12 (cloud 2), when a vertically thin and short (along wind) liquid cloud layer was penetrated numerous times along and against the wind direction

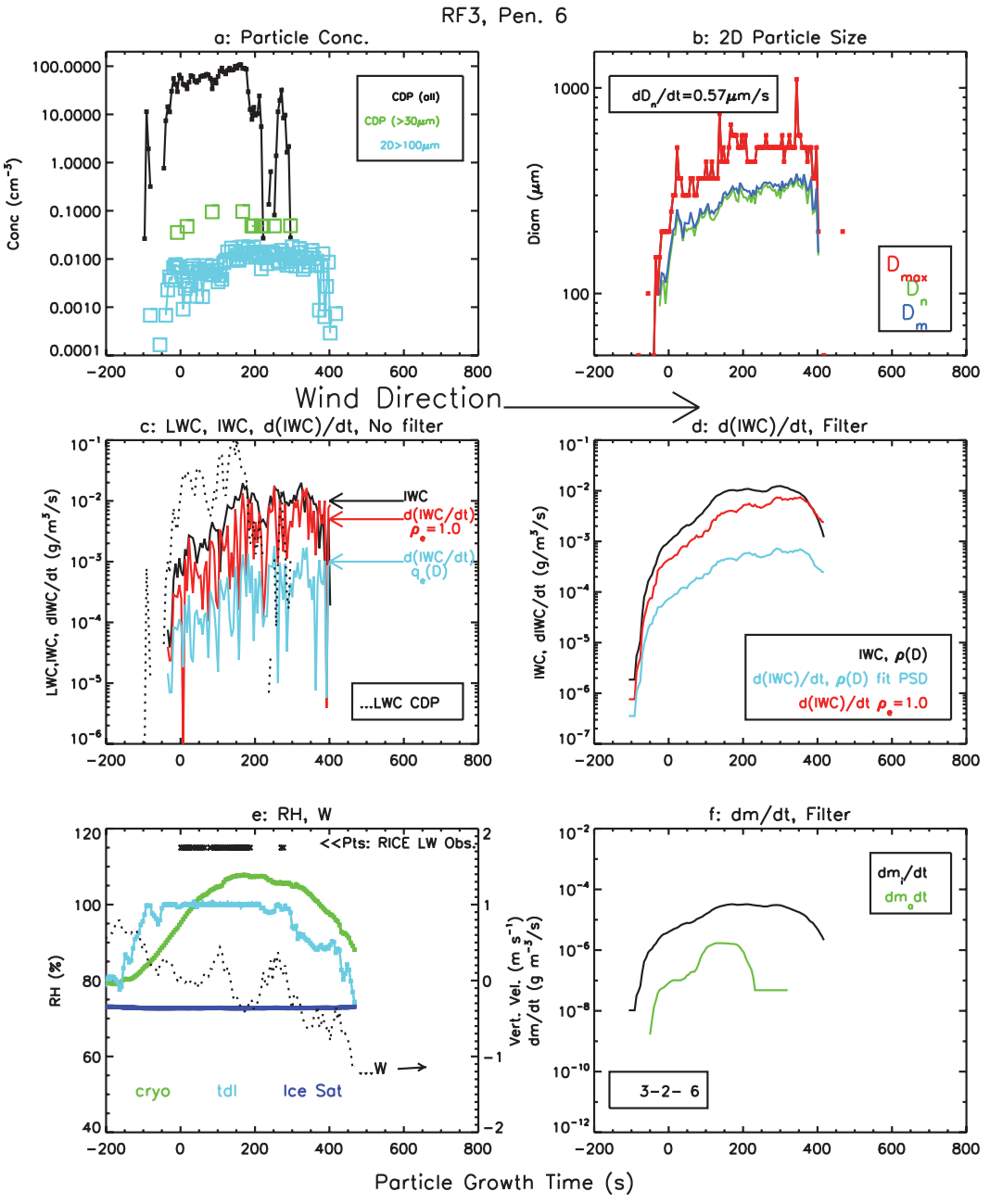

FIG. 13. Example of data collected during a penetration through a wave cloud during RF03: cloud 2, penetration 6. Times are derived along the wind (direction shown with arrow), as discussed in the text. (a) Concentrations from droplet probes. (b) Number and mass weighted mean diameters D_n and D_m and maximum diameter $D_{\max}$ from fast 2DC probe, with penetration-average rate of increase of D with time shown. (c) LWC from the CDP probe and ice water content derived from the PSDs and density–size relationship [Eq. (2)], and time derivatives of the IWC and water content assuming spherical liquid particles [legend shown in (d)]. (d) As in (c), but filtered with a 20-point filter. (e) Left axis: RH measured by the Buck hygrometer and TDL probes and where the RICE probe shows the presence of liquid water (Calcs); right axis: vertical velocity. (f) Diffusion and accretion growth rates of particles sampled at each 1 s by the 2DC probe, using equations developed in the appendix.

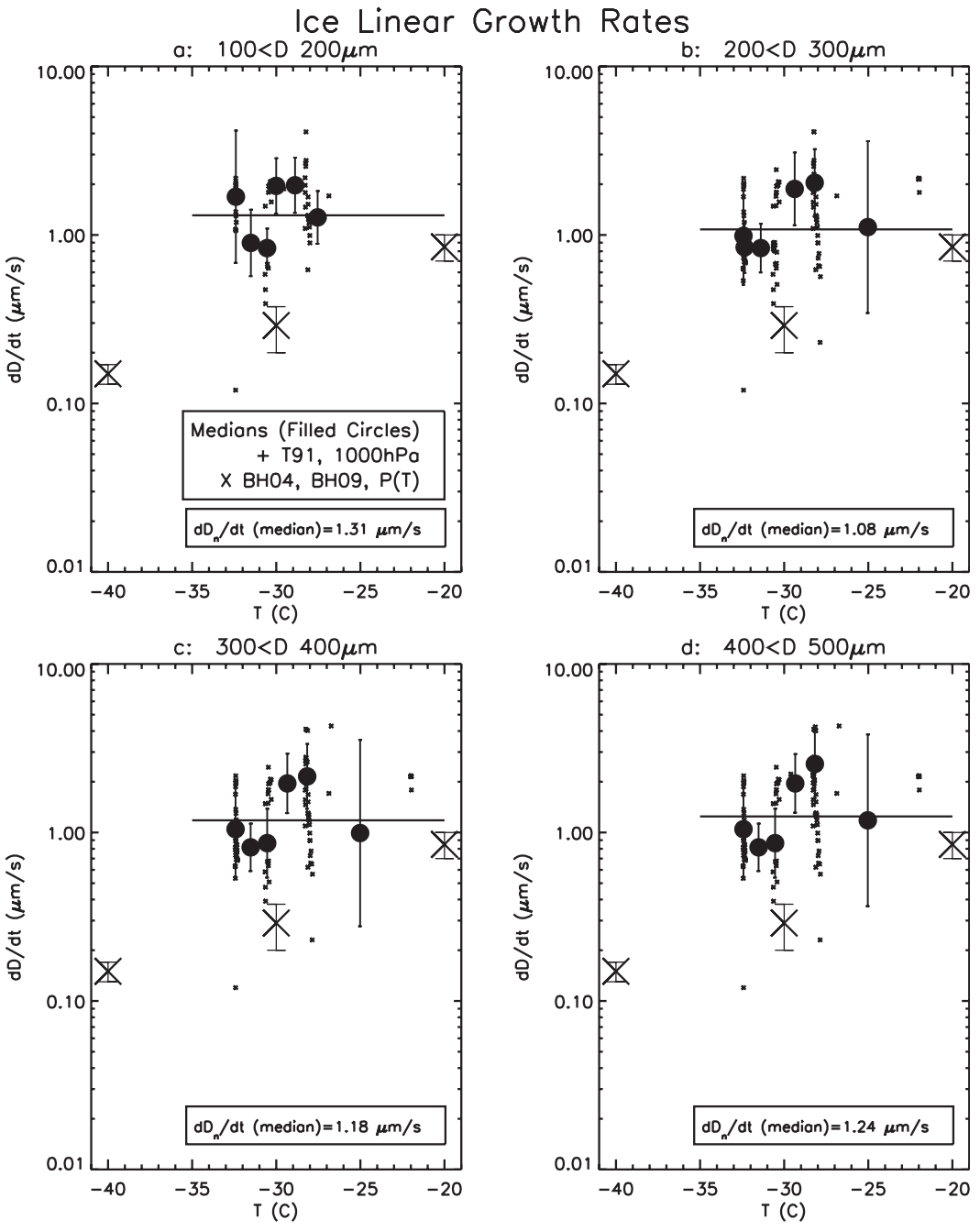

FIG. 14. Linear growth rates derived from the subset of penetrations meeting the criteria described in the text, plotted as a function of temperature in intervals of the mean number-weighted maximum diameter D_n listed at the top of each panel. Each data point is derived from the change in the growth rate over 1 s of aircraft time or about 5 s of growth time. Error bars and standard deviations are shown. Results from laboratory studies are shown where possible.

(Figs. 15 and 16). Although there was a broad region of updraft upwind of the liquid cloud layer, condensation occurred near the crest of the wave (Figs. 16a–d and 17, left panels), with the active ice production and growth layer occurring in a vertically thin layer (Fig. 15), presumably where the air trajectories were relatively flat. Total ice concentrations increased downwind from the edge of the liquid cloud (Fig. 17, left panels), and transit

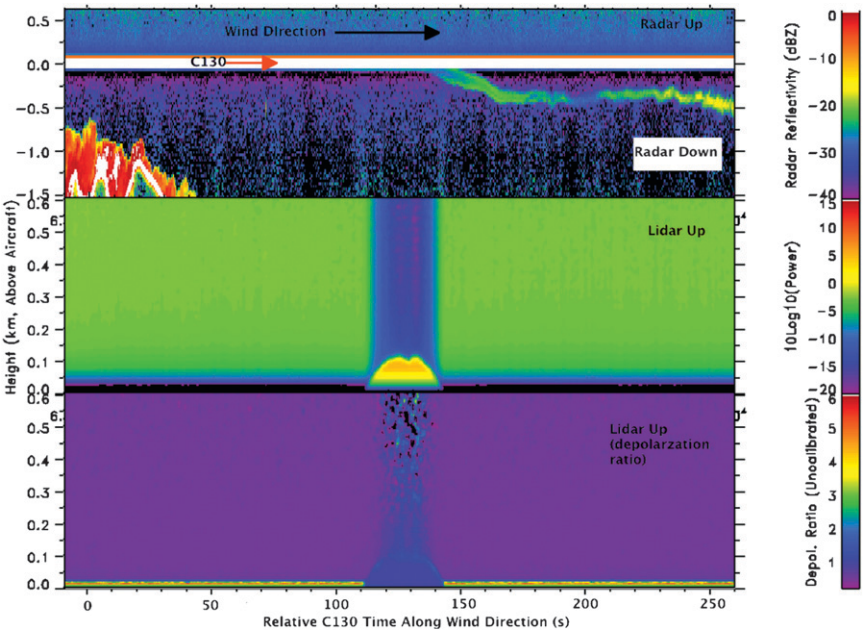

FIG. 15. Radar and lidar observations obtained during upwind penetration (pen. 4) for the second cloud sampled during RF12, from 1831:31 (right) to 1836:00 UTC (left). The winds are from right to left in the figure (the aircraft headed in a direction from downwind to upwind). (top) Radar reflectivity as a function of time, shown at distance above and below the aircraft; the C-130 path is at a height of 0 km. (middle) Lidar backscattered power (relative), with the lidar looking upward, as a function of time. (bottom) Lidar depolarization ratio, viewing upward.

times of the air through the liquid cloud are only about 170 s (Fig. 17, left). The maximum crystal size in the penetrations was approximately 250 μm.

We use the PSDs from this case to estimate the linear growth rates. Given that there was no ice observed upwind of the liquid cloud and the concentrations ramped up quickly after the first 100-μm 2D probe particles were observed, we can estimate the time to reach 100 μm as the approximate time from the leading liquid cloud edge; linear growth rates were about 1 μm s^{-1} (see Fig. 16). If we use the first detection of 2D particles (about 50 μm) at the leading cloud edge and consider growth times in the spatial distance to the first detection of 100-μm particles, we also find comparable growth rates. The first particles were observed with the CPI probe further downstream than for the 2D particles; this is due to the much larger sample volume of the 2DC over the CPI probe. Of course, it is also possible that some small ice particles may have been carried upward to the aircraft level along trajectories, where they were then sampled by the 2D probes. However, the trajectories are nearly flat within the liquid cloud layer and air transit times are short. Assuming that the 100-μm particles became those observed in larger bins, we can shift the concentrations in those bins until the time at which they approximately match the concentrations in the 100-μm bin. The change in the particle size between midpoints of the bins and the time shift yields the approximate growth rates. Although there are a number of error sources in these estimates, they yield approximate linear growth rates on the order of 1 μm s^{-1}.

2) MASS GROWTH RATES

The time rate of increase of the ice water content downwind of the leading cloud edge should equate to the mass growth rate of the ice particle population, assuming that the penetration is approximately along the airflow (streamlines). This section compares the observed and calculated rates of increase in the IWC during penetrations to determine whether the observations are consistent with this conceptual view.

For each 1-s PSD, we calculate the IWC from

$$\mathrm{IWC}(\mathrm{g\,m^{-3}}) = \sum N_l m_i, \qquad (1)$$

where the summation of the concentrations per size bin N_i is across all size bins; and the particle mass is given by $m = (\pi/6)D^3\rho_e$, where the effective density is taken to be

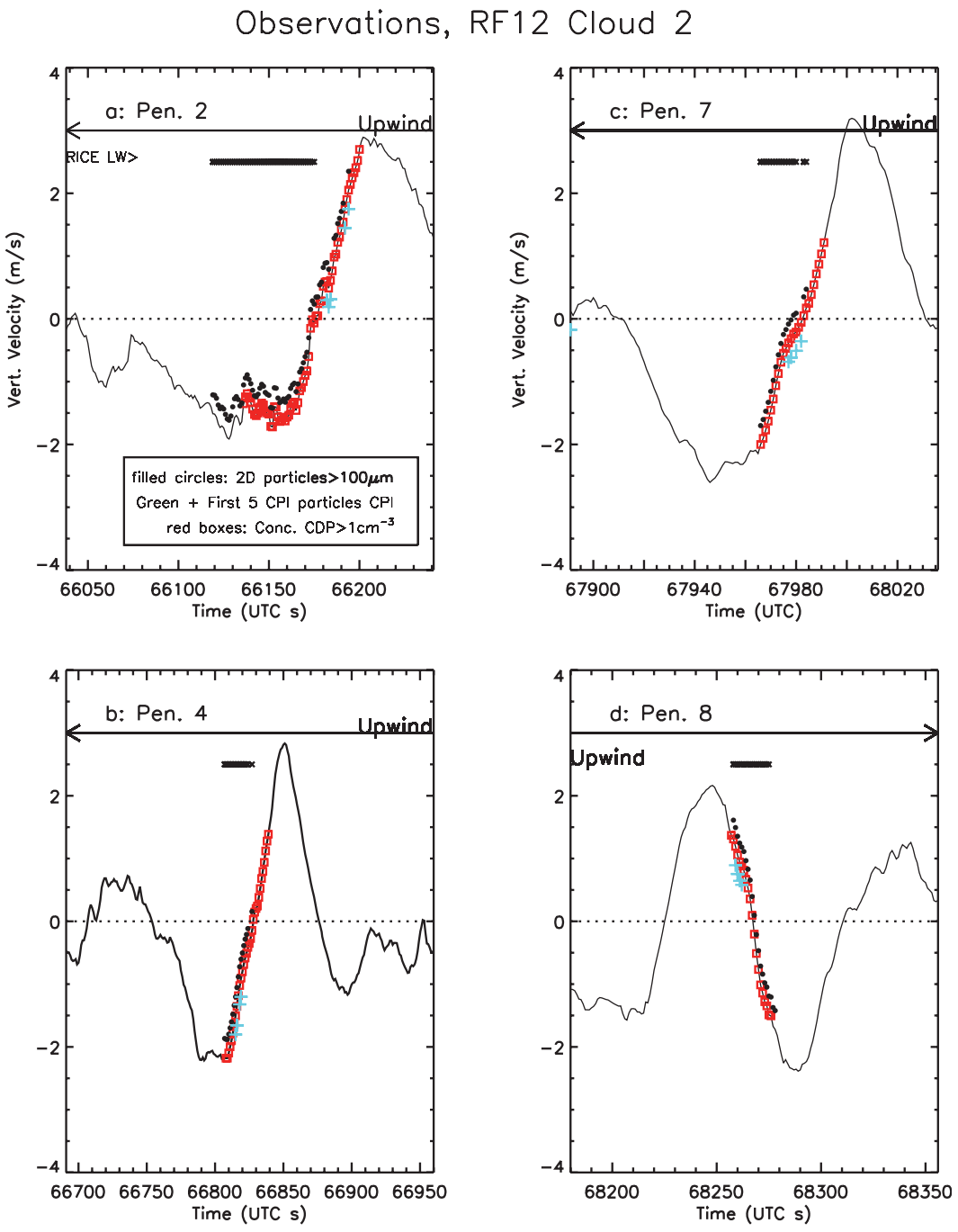

FIG. 16. Vertical velocities vs time during four penetrations along or against the wind in RF12. Locations where 2D probe particles 100 μm and above, cloud droplets as measured by the CDP and detected by the RICE probe, and the first five CPI particles were detected are shown along the vertical velocity traces.

$$\rho_e(\mathrm{g\,cm^{-3}}) = 0.0056D(\mathrm{cm})^{-1.1}. \quad (2)$$

Equation (2) derives from the relationship tested by Brown and Francis (1995) and yields their $m(D)$ relationship. This relationship tests well against direct measurements of the IWC when applied to PSDs for ice-only and mixed-phase clouds generated by large-scale lift (and not convection) at temperatures of −10°C and below, not unlike the ICE-L conditions. Equation (2) yields densities that are above 0.91 g cm^{-3} for sizes below 97 μm; ρ_e is capped at 0.91 g cm^{-3}.

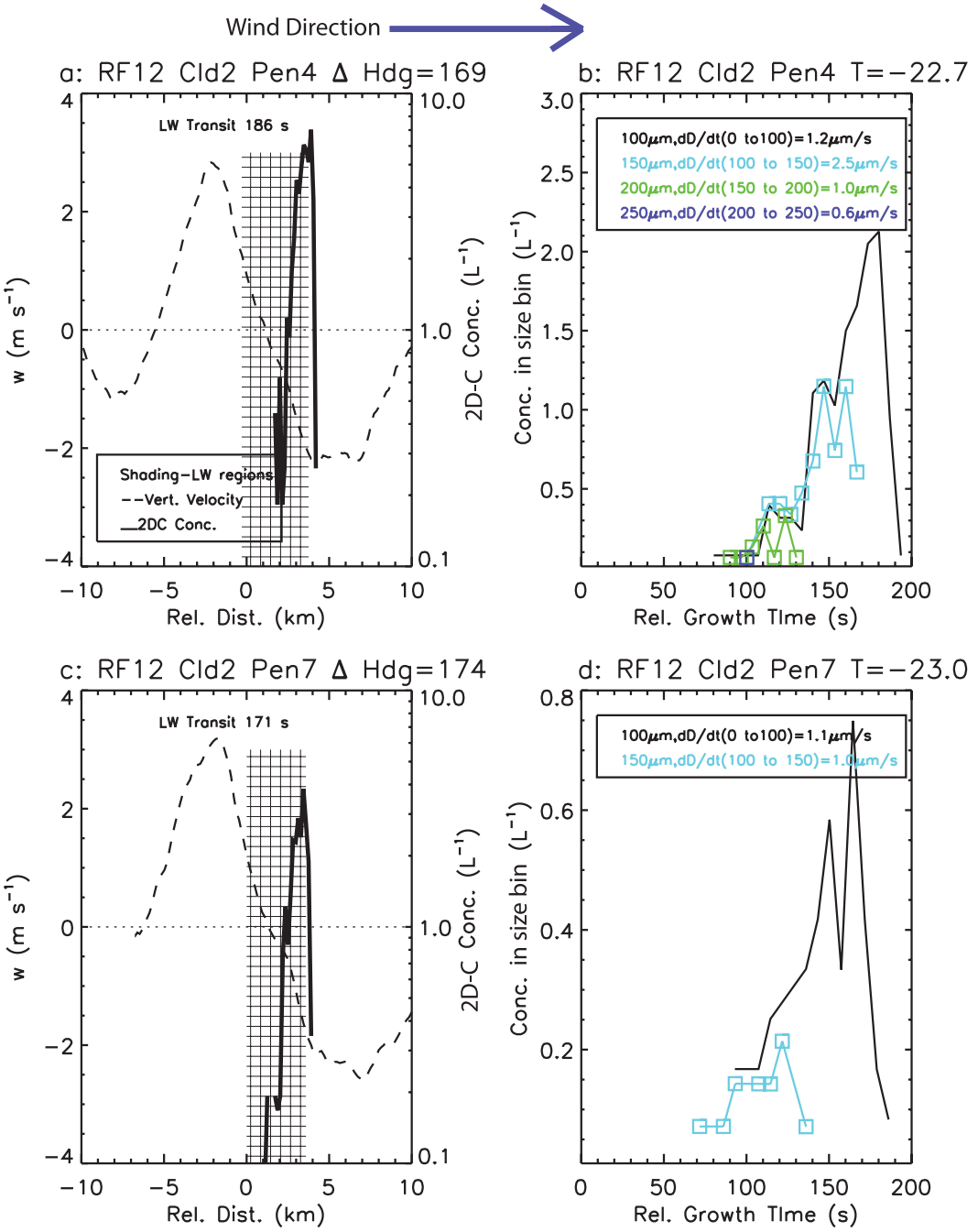

FIG. 17. Observations and analysis of the ice concentrations with distance from upwind to downwind for two penetrations from the second cloud sampled during RF12. Temperatures range from −20.6° to −24.6°C. (left) Vertical velocity (dashed, left axis) and ice concentration (>100 μm solid, right). Hatched regions show locations of liquid water. Relative distance (abscissa) is distance relative to the first detection of liquid cloud. (right) Size-dependent concentrations, color coded as shown, with those sizes 150 μm and above shifted to the left by the time needed to fit the observations for the first (100 μm) size bin, yielding a growth rate. The growth rate derived for the 100-μm bin is the time required for the first detection of particles in that size bin. Relative growth time (abscissa) is time along wind from the left axis, with the liquid edge at a time of about 100 s.

The IWCs for both mixed-phase and ice-only regions are calculated using Eqs. (1) and (2) (Fig. 13c). CVI data are not used to estimate the IWCs because of concerns about the CVI enhancement and shadowing calculations on the C-130 and further because the CVI CWCs are mostly dominated by the LWCs for more than 80% of the periods intensively studied. These IWCs are smoothed to reduce statistical fluctuations caused by the use of 1-Hz data (Fig. 13d); short growth times rather than long-term averaging are needed to reduce uncertainties related to crossing streamlines. Time derivatives of the smoothed IWCs, at 1-s C-130 time increments, are used to derive the rates of increase of the IWCs (Fig. 13d).

The calculated rate of increase in the IWC with distance downwind (the mass growth rate of the ice particle population) was compared to the mass growth rates for the same population of particles derived from theory (Fig. 13f). For simplicity, we assume that ice particles grow spherically, with a shape factor (capacitance) taken to be $C = 0.3D$ [after Westbrook et al. (2008) for plates and rosettes with aspect ratios of <3] and consider the enhancement in growth due to ventilation (see the appendix). An estimate of the ice supersaturation and hence the relative humidity is needed for the calculations. In liquid water regions as determined by the RICE data, it was assumed that the RH was 100% with respect to water (Fig. 13e, Calcs, a reasonable first approximation). Growth rates through accretion are considered, using the measured droplet size distributions to estimate collection efficiency and the liquid water contents; these rates were typically an order of magnitude below the mass rates and are not considered further. This conclusion is also reached by viewing the CPI particle imagery for the cases studied and is largely supported by observations in wave clouds of the onset size for riming of columns and rosettes. Baker and Lawson (2006) showed that the onset size for riming onset for columns is about 150–300-μm length (width is a better predictor of this size but not how our data are analyzed) and for rosettes is 100–300 μm in maximum dimension. Significant riming, contributing significantly to mass, occurs when pristine ice reaches 200–400 μm, depending on the habit. Therefore, our mass estimates based primarily on diffusion growth are valid for the early growth (out to 200–400 μm), which comprises most instances we have studied.

The IWCs and mass growth rate calculations rely on the measured PSDs; therefore, errors in the measurement of the PSDs affect both calculations in the same way. The theoretical expressions are developed in terms of ice mass growth rates and do not assume an ice mass density. Because the IWCs are derived from the assumed effective density, errors in the effective density would show up in the calculated IWCs but not the growth rates.

The ice mass growth rates via diffusion as derived from theory are uniformly smaller than the time rate of increase in the IWC (Fig. 18a). We attribute the factor of 4+ discrepancies between the theoretical rates and the rate of increase in the calculated IWC (see dashed line, Fig. 18a) to be largely due to low densities of the ICE-L particles at small sizes. The capacitance term might be in error but is not likely to be a factor of 4 too large.

If the mass growth rate calculations are accurate, they provide a means of estimating the effective densities. Specifically, the time rate of increase in the IWC should correspond to the calculated dm/dt. In Fig. 18b, the effective densities that agree with the calculations are estimated. Values for $\rho_e \sim 0.05$ g cm^{-3} are much lower than those found in the ice-only regions where direct IWC measurements were made, and they are about half of those found by RWS76 and T91 at temperatures near -20°C and by BH04 at lower temperatures.

By applying these ice densities to linear growth rate calculations, we find a good match between calculated linear growth rates and the observed values, providing a consistency between calculated mass growth rates and IWCs, and calculated and observed linear growth rates. We therefore conclude that the ice densities are smaller than those derived from the PSDs and measured IWCs in the sublimation regions of the wave clouds.

b. *Locations and rates of ice nucleation*

It is very difficult to demonstrate whether ice nucleation is time dependent in natural clouds from laboratory observations because the mix of ice nuclei used in the laboratory might not be representative of natural conditions. The increase in the fraction of the total ice concentrations observed with distance downwind of the liquid water edge for the very simple case associated with RF12 could suggest that ice nucleation is time dependent, occurring over periods of 150 s (Fig. 19a). Alternatively, this increase with downwind distance could also be due to differential growth rates, since polycrystalline forms were observed together with columns (Fig. 12, RF12).

We explore the differential growth hypothesis to see if it can explain the observations shown in Fig. 19a. Each 1-s PSD across the two RF12 penetrations is used to estimate where the particles could have originated, with different assumed growth rates. Taking the particle size to correspond with the midpoint of the first reliable size bin (75–125 μm), we trace back where that concentration may have originated. We use four linear diameter D versus time t relationships for the backtracked trajectory calculations, where time is converted to negative distance using the mean wind speed across the penetration.

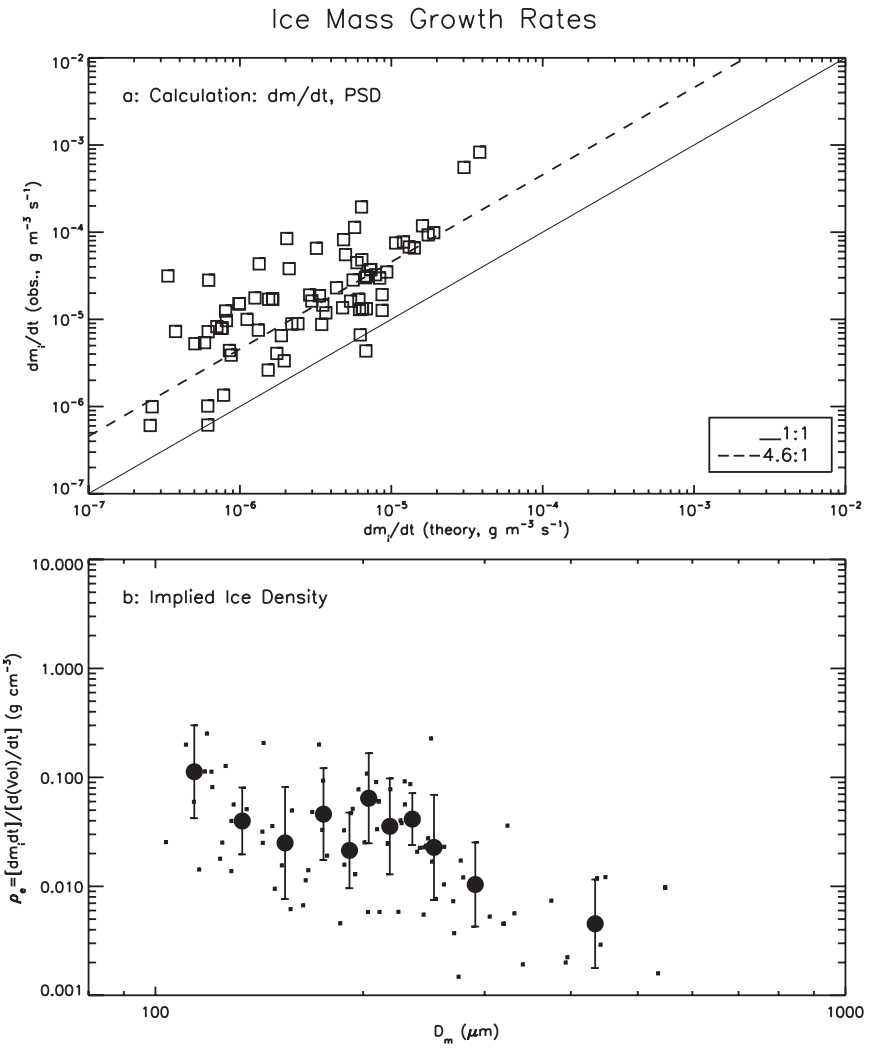

FIG. 18. (a) Mass growth rates derived from measurements compared to theory. Points are selected as in Fig. 14. Temperatures range from −21° to −32°C. Lines showing 1:1 curve and median value of the discrepancies are shown. (b) Ice particle effective density required for the theory and observations to agree.

As input into the mass and linear growth rate calculations in the appendix, we assume constant temperatures from −20° to −35°C, a relative humidity of 100%, a pressure–temperature T relationship developed from the ICE-L dataset to derive the pressure $f(T)$, and an ice effective density to be given by Eq. (2). Note that the ρ_e values are 0.91 g cm^{-3} throughout almost the entire 0–100-μm size range. The following two relationships express the results of the linear growth rate calculations from the appendix assuming a density given by Eq. (2):

(a) $D = (1.64 - 0.0374T)t^{0.61}$ called Assumption-1.

The following equation is as in (a), but for $\rho_e = 0.1$ g cm^{-3} for all sizes, yielding

(b) $D = (22.16 + 0.261T)t^{0.49}$ called Assumption-2.

The following two expressions assume constant linear growth rates expressing the bounds of the results from the observations:

(c) $D = (1.4\,\mu\text{m s}^{-1})t$ called Assumption-3,

(d) $D = (0.7\,\mu\text{m s}^{-1})t$ called Assumption-4, one-half that amount given by (c).

Differential growth rates bounded by (c) and (d) are used to account for habit variability—polycrystalline forms observed together with columns (Fig. 12, RF12)—and the spread observed in the linear growth rates (Fig. 14). To

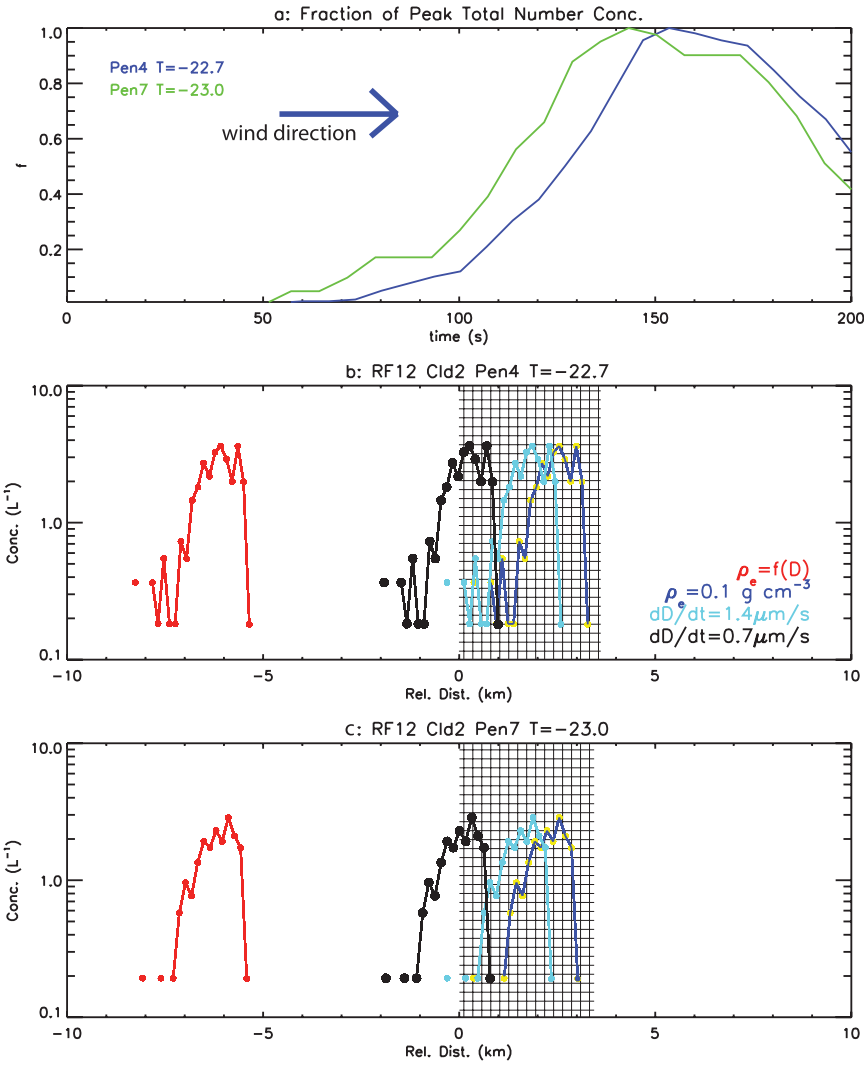

FIG. 19. Observations and calculations of the ice concentration with distance from upwind to downwind for two penetrations from the second cloud sampled during RF12. (a) Fraction of peak total concentration as a function of time from the leading cloud edge. Backtracked starting positions of particles observed in the 100 (75–125)-μm size bin, shown as a function of the observed concentration for penetration (b) 4 and (c) 7. Starting position and concentration of particles observed in 100 (75–125)-μm size bin for each 1-s PSD, backtracked assuming four linear growth rates. Hatched regions show locations of liquid water.

grow to 100 μm, an ice crystal at $T = -22$°C will require (a) 430, (b) 40, (c) 71, and (d) 142 s, corresponding to average growth rates of 0.23, 2.5, 1.4 and 0.7 μm s^{-1}, respectively.

Figures 17b and 17c show the calculated starting positions of the 100-μm particles as a function of their concentration observed through the penetrations. As shown in Fig. 15, this is a case where the air trajectories are nearly flat; at the crest of the wave. Assumption-1 is inconsistent with the observations: the ice particles would have had to originate far upstream of the first remotely sensed locations of hydrometeors at the leading liquid cloud edge. Assumption-2 is plausible, but the crystals do not begin at the leading edge where ice nucleus measurements (Part II) suggest that ice crystals should have been produced as soon as water saturation was reached. Growth rates via that assumption are therefore too fast. Assumption-3 and -4 produce results that can explain the observations: the first ice observed could have had high linear growth rates and slower rates accounted for most of the ice.

In summary, although we cannot rule out delayed nucleation as the factor responsible for the steady increase

in the total number concentration with distance downwind, variability in the growth rates by only a factor of 2 and the associated habit variations can fully account for the increase in the total number concentration with distance into the liquid water region.

4. Summary and conclusions

Orographic wave clouds can provide a natural, laboratory-like environment for the study of microphysical processes and for evaluating measurements from airborne probes over a wide range of temperatures and pressures. With well-posed research problems and instrumentation designed to provide the required measurements, significant progress can be made in tackling problems that are difficult to measure in the laboratory.

Here, lenticular wave clouds are used to estimate the linear and mass growth rates of ice particles, at temperatures from −20° to −32°C and pressures from 400 to 600 hPa, where laboratory observations of growth rates for freely suspended ice particles have not been conducted, and to deduce the rate of ice production at nearly constant temperatures and at water saturation at a nearly constant temperature, a challenging laboratory measurement problem. A distinction should be made, however, in that the light riming of the wave cloud crystals above the threshold size for riming could have enhanced the diffusional growth of thin ice structures with higher linear growth rates. For the early growth of ice particles—out to 300 or 400 μm in maximum diameter when riming in supercooled cloud could become significant—ice crystal growth rates measured in wave clouds may apply to a broad range of supercooled clouds globally (adjusted for atmospheric pressure), just as would observations in the laboratory. The observations would not apply to vigorous convection where ice crystals are transported through wide temperature ranges during their early growth.

Linear growth rates for particles from about 100 to 400 μm are found to be larger than expected, which we conclude is due to ice particle effective densities that are lower than have been assumed by extrapolation of earlier observations for warmer temperatures (e.g., RWS76) and through use of the widely used Brown and Francis (1995) relationship. The low densities may be accounted for by thin, elongated ice structures that develop from light riming on the surfaces of the ice particles, leading to side plane–type ice crystals, with the randomness of the process leading to a spectrum of ice particle densities for a given particle size. To use wave clouds as a means of determining linear growth dimensions for the first 100–200 μm of growth requires high-resolution images of the ice particles, now possible with such probes as the 2DS (Lawson et al. 2006). Also required are accurate values of the mass of <200-μm particles, something that cannot be readily achieved with probes such as the CVI as configured because they are not sensitive enough to detect very low values of the ice water content and cannot readily differentiate ice from liquid. Having a CVI with a longer-path water vapor sensor and a dual ''cut'' (minimum detectable) size could provide this capability. Collecting ice particles on oil-coated slides, as has been performed previously (Cooper and Vali 1981), could surmount this problem. Mass growth rates can be compared directly to theory, but again the limitation is not being able to measure the ice water content directly; directly collecting ice particles could provide the needed information. The use of remote sensing data—such as upward- and downward-viewing lidar and radar that are well calibrated—could be used to provide some of the necessary information, at least when both are able to detect the thin ice layers and tails that develop from wave clouds.

Differentiating variability in growth rates and the rates of ice nucleation with isothermal conditions and water saturation requires high-resolution cloud particle imagery with well-characterizable sample volumes and instruments that can sample ice nuclei either in situ or upwind of cloud layers and expose the nuclei to varying periods in liquid water regions. Both factors can lead to significant broadening of the particle size distributions and are therefore important measurements for improving the representation of ice growth processes in models. Although we can account for the apparent increase in particle concentration with transit time in the liquid water regions by a factor of 2 variance in ice growth rates, we were unable to derive the contribution because of delayed ice nucleation rates.

Acknowledgments. The authors wish to thank the National Science Foundation for their support of the research reported in this article and to the NCAR Aviation Facility pilots, engineers, and crew, especially Jorgen Jensen, for their support throughout this project. We wish to thank T. Takahashi for providing original laboratory data. CT was funded by NSF through Grant ATM-0612605.

APPENDIX

Ice Diffusion and Accretion Growth Rates

Mass and linear growth rates can be derived from (see Pruppacher and Klett 1997, hereafter PK97):

$$dm_i/dt = 4\pi CG' S_i F, \tag{A1}$$

$$dm_a/dt = A_c E(\mathrm{LWC}) V_t. \tag{A2}$$

where dm_i/dt and dm_a/dt are the growth rates through diffusion and accretion, respectively, for single particles, C is the ice crystal shape factor, G' a temperature- and pressure-dependent parameter, and F the ventilation coefficient (see PK97); also, A_c is the cross-sectional area, E the collection efficiency of the ice particles for droplets (size dependent, see PK97), D the maximum particle dimension, and V_t the terminal velocity. As an approximation, $C \approx 0.3D$ (Westbrook et al. 2008).

The value of ρ_e, the ice effective density (crystal mass/volume), can be represented in power-law form as $\rho_e = \alpha D^{\beta}$ [see Eq. (2)]. If we assume that dm_a/dt is generally small compared to dm_i/dt in the wave cloud penetrations and ρ_e is not time dependent, then

$$dD/dt = [6/(\pi\alpha\beta D^{\beta-1})]\, dm_i/dt. \quad \text{(A3)}$$

For a population of ice particles, the linear and mass growth rates can be written as

$$dm_i/dt = 4\pi G' S_i \Sigma N_l C_i F_i \quad \text{and} \quad \text{(A4)}$$

$$dD/dt = [6/(\pi\alpha\beta D^{\beta-1})]\, dm/dt, \quad \text{(A5)}$$

where N_i is the concentration of particles in size bin i and the summation is taken over all size bins i. The parameters need to calculate the ventilation coefficient and collection efficiency are presented in PK97.

REFERENCES

Bailey, M., and J. Hallett, 2004: Growth rates and habits of ice crystals between −20° and –70°C. *J. Atmos. Sci.,* **61,** 514–544.

——, and ——, 2009: A comprehensive habit diagram for atmospheric ice crystals: Confirmation from the laboratory, AIRS II, and other field studies. *J. Atmos. Sci.,* **66,** 2888–2899.

Baker, B. A., and R. P. Lawson, 2006: In situ observations of the microphysical properties of wave, cirrus, and anvil clouds. Part I: Wave clouds. *J. Atmos. Sci.,* **63,** 3160–3185.

Brown, P. R. A., and P. N. Francis, 1995: Improved measurements of the ice water content in cirrus using a total-water probe. *J. Atmos. Oceanic Technol.,* **12,** 410–414.

Connolly, P. J., M. J. Flynn, Z. Ulanowski, T. W. Choularton, M. W. Gallagher, and K. N. Bower, 2007: Calibration of the cloud particle imager probes using calibration beads and ice crystal analogs: The depth of field. *J. Atmos. Oceanic Technol.,* **24,** 1860–1879.

Cooper, W. A., and G. Vali, 1981: The origin of ice in mountain cap clouds. *J. Atmos. Sci.,* **38,** 1244–1259.

Davis, S., L. M. Avallone, E. M. Weinstock, C. H. Twohy, J. B. Smith, and G. L. Kok, 2007: Comparisons of in-situ measurements of cirrus cloud ice water content. *J. Geophys. Res.,* **112,** D10212, doi:10.1029/2006JD008214.

DeMott, P. J., D. C. Rogers, S. M. Kreidenweis, Y. Chen, C. H. Twohy, D. Baumgardner, A. J. Heymsfield, and K. R. Chan, 1998: The role of heterogeneous freezing nucleation in upper tropospheric clouds: Inferences from SUCCESS. *Geophys. Res. Lett.,* **25,** 1387–1390.

——, K. Sassen, M. R. Poellot, D. Baumgardner, D. C. Rogers, S. D. Brooks, A. J. Prenni, and S. M. Kreidenweis, 2003: African dust aerosols as atmospheric ice nuclei. *Geophys. Res. Lett.,* **30,** 1732, doi:10.1029/2003GL017410.

——, and Coauthors, 2010: Predicting global atmospheric ice nuclei distributions and their impacts on climate. *Proc. Natl. Acad. Sci. USA,* **107,** 11 217–11 222, doi:10.1073/pnas.0910818107.

Durant, A. J., and R. A. Shaw, 2005: Evaporation freezing by contact nucleation inside-out. *Geophys. Res. Lett.,* **32,** L20814, doi:10.1029/2005GL024175.

Eidhammer, T., and Coauthors, 2010: Ice initiation by aerosol particles: Measured and predicted ice nuclei concentrations versus measured ice crystal concentrations in an orographic wave cloud. *J. Atmos. Sci.,* **67,** 2417–2436.

Field, P. R., and Coauthors, 2001: Ice nucleation in orographic wave clouds: Measurements made during INTACC. *Quart. J. Roy. Meteor. Soc.,* **127,** 1493–1512.

——, A. J. Heymsfield, and A. Bansemer, 2006: Shattering and particle interarrival times measured by optical array probes in ice clouds. *J. Atmos. Oceanic Technol.,* **23,** 1357–1371.

Gerber, H., C. H. Twohy, B. Gandrud, A. J. Heymsfield, G. M. McFarquhar, P. J. DeMott, and D. C. Rogers, 1998: Measurements of wave-cloud microphysical properties with two new aircraft probes. *Geophys. Res. Lett.,* **25,** 1117–1120.

Heymsfield, A. J., and L. M. Miloshevich, 1995: Relative humidity and temperature influences on cirrus formation and evolution: Observations from wave clouds and FIRE II. *J. Atmos. Sci.,* **52,** 4302–4326.

King, W. D., 1984: Air flow and particle trajectories around aircraft fuselages. I. Theory. *J. Atmos. Oceanic Technol.,* **1,** 5–13.

Lawson, R. P., D. O'Connor, P. Zmarzly, K. Weaver, B. A. Baker, Q. Mo, and H. Jonsson, 2006: The 2D-S (stereo) probe: Design and preliminary tests of a new airborne, high-speed, high-resolution particle-imaging probe. *J. Atmos. Oceanic Technol.,* **23,** 1462–1477.

Mazin, I. P., A. V. Korolev, A. J. Heymsfield, G. A. Isaac, and S. G. Cober, 2001: Thermodynamics of icing cylinder for measurements of liquid water content in supercooled clouds. *J. Atmos. Oceanic Technol.,* **18,** 543–558.

Norment, H. G., 1988: Three-dimensional trajectory analysis of two drop sizing instruments: PMS OAP and PMS FSSP. *J. Atmos. Oceanic Technol.,* **5,** 743–756.

Pratt, K. A., and Coauthors, 2010: Observation of playa salts as nuclei of orographic wave clouds. *J. Geophys. Res.,* **115,** D15301, doi:10.1029/2009JD013606.

Pruppacher, H. R., and J. D. Klett, 1997: *Microphysics of Clouds and Precipitation*. 2nd ed. Kluwer Academic, 954 pp.

Reinking, R. F., 1979: The onset and early growth of snow crystals by accretion of droplets. *J. Atmos. Sci.,* **36,** 870–881.

Ryan, B. E., E. R. Wishart, and D. E. Shaw, 1976: The growth rates and densities of ice crystals between −3° and −21°C. *J. Atmos. Sci.,* **33,** 842–850.

Strapp, J. W., and Coauthors, 2003: Wind tunnel measurements of the response of hot-wire liquid water content

instruments to large droplets. *J. Atmos. Oceanic Technol.,* **20,** 791–806.

Takahashi, T., and N. Fukuta, 1988: Supercooled cloud tunnel studies on the growth of snow crystals between −4° and −20°C. *J. Meteor. Soc. Japan,* **66,** 841–855.

——, T. Endoh, G. Wakahama, and N. Fukuta, 1991: Vapor diffusional growth of free-falling snow crystals between −3° and −23°C. *J. Meteor. Soc. Japan,* **69,** 15–30.

Twohy, C. H., and M. R. Poellot, 2005: Chemical characteristics of ice residual nuclei in anvil cirrus clouds: Evidence for homogeneous and heterogeneous ice formation. *Atmos. Chem. Phys.,* **5,** 2289–2297.

——, A. J. Schanot, and W. A. Cooper, 1997: Measurement of condensed water content in liquid and ice clouds using an airborne counterflow virtual impactor. *J. Atmos. Oceanic Technol.,* **14,** 197–202.

——, J. W. Strapp, and M. Wendisch, 2003: Performance of a counterflow virtual impactor in the NASA Icing Research Tunnel. *J. Atmos. Oceanic Technol.,* **20,** 781–790.

——, and Coauthors, 2010: Relationships of biomass burning aerosols to ice in orographic wave clouds. *J. Atmos. Sci.,* **67,** 2437–2450.

Westbrook, C. D., R. J. Hogan, and A. J. Illingworth, 2008: The capacitance of pristine ice crystals and aggregate snowflakes. *J. Atmos. Sci.,* **65,** 206–219.